Spring 2014

A NOVEL THREE DEGREE-OF-FREEDOMS OSCILLATION SYSTEM OF INSECT FLAPPING WINGS

Yi Qin
Purdue University

Graduate School ETD Form 9
(Revised 01/14)

PURDUE UNIVERSITY
GRADUATE SCHOOL
Thesis/Dissertation Acceptance

This is to certify that the thesis/dissertation prepared

By Yi Qin

Entitled

A NOVEL THREE DEGREE-OF-FREEDOMS OSCILLATION SYSTEM OF INSECT FLAPPING WINGS

For the degree of Master of Science in Mechanical Engineering

Is approved by the final examining committee:

Xinyan Deng

Bin Yao

Justin E. Seipel

To the best of my knowledge and as understood by the student in the *Thesis/Dissertation Agreement. Publication Delay, and Certification/Disclaimer (Graduate School Form 32)*, this thesis/dissertation adheres to the provisions of Purdue University's "Policy on Integrity in Research" and the use of copyrighted material.

Xinyan Deng

Approved by Major Professor(s): _____

_____

Approved by: David C. Anderson 04/09/2014

Head of the Department Graduate Program Date

A NOVEL THREE DEGREE-OF-FREEDOMS OSCILLATION SYSTEM OF INSECT FLAPPING WINGS

A Thesis

Submitted to the Faculty

of

Purdue University

by

Yi Qin

In Partial Fulfillment of the

Requirements for the Degree

of

Master of Science in Mechanical Engineering

May 2014

Purdue University

West Lafayette, Indiana

ACKNOWLEDGEMENTS

I would like to thank my family for their support and encouragement in the pursuit of my education. Without it, I would not be capable of reaching the goals I have set out to achieve.

TABLE OF CONTENTS

Page

LIST OF TABLES v

LIST OF FIGURES vi

ABSTRACT viii

CHAPTER 1. INTRODUCTION 1

1.1 Background 1

1.2 Flight Muscles 3

1.3 Scope and Outline of Thesis 6

CHAPTER 2. DYNAMIC MODELING OF FLAPPING WINGS 8

2.1 Coordinate Definitions 8

2.2 Model of Flight Muscles 11

2.3 Wing Morphology 12

2.4 Blade-Element Model 15

2.4.1 Translational Force 19

2.4.2 Rotational Force 22

2.4.3 Rotational Damping Moment 24

2.5 Equation of Motion 26

2.6 Dimensional Analysis 27

2.7 Lift-to-Weight Ratio and Forces Coefficients 29

2.8 Hovering Efficiency 30

2.9 Stroke Cycle 31

CHAPTER 3. SIMULATION OF FLAPPING WINGS 32

3.1 Numerical Simulation of Nonlinear Differential Equations 32

3.2 Parameter Space Search 33

Page

CHAPTER 4. OPTIMIZATION OF FLAPPING WINGS 44
4.1 Optimization Technique 45
4.2 Genetic Algorithms Setup 49
4.3 Nelder-Mead Simplex Algorithm Setup 56
4.4 Optimization Results 63
CHAPTER 5. CONCLUSION 73
LIST OF REFERENCES 74
APPENDICES
Appendix A Non-dimensional Aerodynamic Moment 81
Appendix B Contour Plots 84
Appendix C Fourier Series 86
VITA 90

LIST OF TABLES

Table Page

Table 2.1. Morphological parameters used for simulation. 15

Table 3.1. Table of stiffness coefficients, lift-to-weight ratio and mean power loading in selected cases. 37

Table 4.1. Table of optimized parameters and their ranges. 46

Table 4.2. Optimization parameters with zero deviation. 65

Table 4.3. Optimization parameters with nonzero deviation. 65

Table 4.4. Selected Fourier coefficients for optimization wing kinematics results with zero deviation. 68

Table 4.5. Selected Fourier coefficients for optimization wing kinematics results with nonzero deviation. 69

Table B.1. Fourier coefficients for optimization wing kinematics results with zero deviation 86

Table B.2. Fourier coefficients for optimization wing kinematics results with non-zero deviation 87

LIST OF FIGURES

Figure Page

Figure 1.1. Wing tip trajectories for bumble bees in hovering flight. 2

Figure 1.2. Synchronous and asynchronous flight muscles. 4

Figure 2.1. Coordinate systems and Euler angles, shown for a left wing and vertical-body orientation. 9

Figure 2.2. Wing platform morphological parameters..... 13

Figure 2.3. An illustration of wing's local angle of attack. 18

Figure 2.4. An illustration of translational forces. 20

Figure 2.5. An illustration of rotational forces. 23

Figure 2.6. Relative velocity profile by the pure rotation of the wing..... 25

Figure 3.1. An illustration of the simulation process. 33

Figure 3.2. Contours of lift-to-weight ratio (a) and mean power loading (b) as functions of deviation stiffness coefficient and rotation stiffness coefficient. 35

Figure 3.3. Four regions in contour of lift-to-weight ratio as functions of deviation stiffness coefficient and rotation stiffness coefficient. 36

Figure 3.4. Wing trajectories of four cases. 38

Figure 3.5. Wing kinematics and aerodynamic force coefficient versus stroke cycle during 40th stroke cycle. 40

Figure 3.6. Wing trajectories portrayed from 31th to 40th stroke cycles. 42

Figure 3.7. Contours of amplitude of the stroke angle as functions of deviation stiffness coefficient and rotation stiffness coefficient. 42

Figure 4.1. A selection of possible wing kinematics. 47

Figure 4.2. Flowchart for the genetic algorithm. 56

Figure 4.3. Stroke stiffness coefficients versus input torque coefficient. 67

Figure Page

Figure 4.4. Wing trajectories, downstroke phases and upstroke phases of optimized wing motions..... 71
Figure 4.5. Wing kinematics and aerodynamic force coefficient for optimized wing motions versus stroke cycle over the 40th stroke cycle. 72
Figure B.1. Contours of amplitude of the stroke angle as functions of deviation stiffness coefficient and rotation stiffness coefficient. 84
Figure B.2. Contours of amplitude of the rotation angle as functions of deviation stiffness coefficient and rotation stiffness coefficient. 85
Figure B.3. Contours of amplitude of the deviation angle as functions of deviation stiffness coefficient and rotation stiffness coefficient. 85

ABSTRACT

Qin, Yi. M.S.M.E., Purdue University, May 2014. A Novel Three Degree-of-Freedoms Oscillation System of Insect Flapping Wings. Major Professor: Xinyan Deng, School of Mechanical Engineering.

We propose an oscillation system to replicate the dynamic behavior of flapping wings, inspired by insect flight muscles. In particular, we study the flight of the fruit fly *Drosophila virilis*. We model the wing as a rigid body with three degree-of-freedom, described by three Euler angles: the stroke angle, the rotation angle and the deviation angle. Insect flight muscles are separated into two types: power muscles and control muscles. One actuator and one torsional spring at the stroke angle act as the power muscles. Two torsional springs at the rotation angle and the deviation angle mimic the control muscles. A dynamic model, using a blade-element model and a quasi-steady model to calculate aerodynamic forces and moments, is set up for analysis of the system's performance. Using non-dimensional analysis, we are able to identify the dynamic behavior of the system through four coefficients: stroke stiffness coefficient, rotation stiffness coefficient, deviation stiffness coefficient and input torque coefficient. We use the dynamic model to explore a large coefficients space of the oscillation system. We find that tuning deviation stiffness coefficient and rotation stiffness coefficient generates four different types of wing trajectories. Among them, the one with a high deviation stiffness coefficient and a mediate rotation stiffness coefficient produces

high lift and high power loading. Its wing trajectory is quite similar to the wing trajectory in actual insects. Furthermore, a hybrid optimization algorithm (a genetic algorithm and a Nelder-Mead simplex algorithm) is implemented to find the optimal stiffness coefficients. Through these coefficients, the system minimizes power loading while still providing enough lift to maintain a time-averaged constant altitude over one stroke cycle. The results of this optimization indicate that the flapping wing with nonzero deviation achieves a better aerodynamic performance than the wing with zero deviation. The oscillatory property of this system does not only explain how insects use flight muscles to tune wing kinematics, but it also allows for design simplifications of the wing driving mechanism of flapping micro air vehicles.

CHAPTER 1. INTRODUCTION

1.1 Background

Throughout the past decades, flapping wing insects attract a lot of attention due to their exceptional flight stability and maneuverability (Dickinson, *et al*., 1999; Fry, *et al.*, 2003; Lentink and Dickinson, 2009; Hedrick, 2009). Many analytical and experimental investigations are made to figure out the mechanisms of aerodynamic force production in flapping insect wings (for reviews, see Lehmann, 2004; Sane, 2003; Viieru, *et al*., 2006). Concepts of flapping flight originated from biology researches inspire the spark of the creation of engineers. They show huge interest in development of flapping wing micro air vehicle (MAVs) that present a large leap forward in agility and maneuverability from traditional fixed and rotary MAVs. However, how to achieve a complex wing trajectory is a myriad of technological and conceptual challenges in designing flapping MAVs. Several have achieved free flight, ranging from larger bird-sized (Pornsin-Sirirak, *et al.*, 2001; Breugel, *et al*., 2008) to smaller insect-sized vehicle (Croon, *et al.,* 2012; Keennon, *et al.*, 2012; Ma, *et al.*, 2013). Among these successful designs, two frequent simplifying assumptions are made. One is that the rotation of the wing is passively assisted by the wing inertia and/or aerodynamic forces, i.e. only the leading edge of the wing is actively controlled. The other is that the stroke plane is flat, i.e. the wing flaps back and forth in a plane showing a line wing tip trajectory, and does not deviate vertically. There are two

reasons for these assumptions: (1) passive rotation and zero deviation greatly simply the actuation mechanism, and (2) simplified wing motions can generate enough lift. Any attempt to achieve complex wing motions such as figure-of-eight or oval shapes, induce additional and unexpected mechanism, thus fail to generate enough lift to support the weight (Banala and Agrawal, 2005; Finio, 2010; Seshadri, *et al.*, 2012).

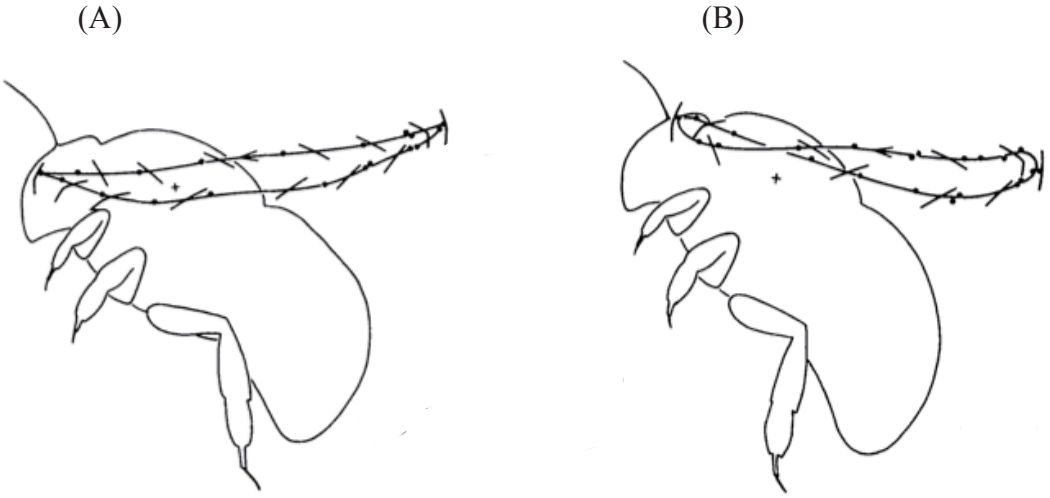

Figure 1.1. Wing tip trajectories for bumble bees in hovering flight. (A) shows the oval shape for the bumbles *Bombus hortorum*, and (B) shows the figure-of-eight for the bumble bee *Bombus lucorum*. Adapted from (Ellington, C. P., 1984b).

Even though these assumptions seen to be a reasonable approximation, insects and hummingbirds do reveal complex wing tip trajectories. Remarkably diversity of wing tip trajectories has been reported in the ladybird *Coccinella 7-punctata*, the crane-fly *Tipula obsolete*, the crane-fly *Tipula paludosa*, the hover-fly *Episyrphus balteatus*, the drone-fly *Eristalis tenax*, the honey bee *Apis mellifera*, the bumble bee *Bombus hortorum* and the bumble bee *Bombus lucorum* (Ellington 1984b; Brodsky, 1994;). Oval shapes and figure-of-eight shapes for bumble bees are shown in Figure 1.1. Biology studies shown that flies

may rapidly change wing kinematics during steering behavior, resulting in the alteration of wing tip trajectories (Tu and Dickinson, 1996). Additionally recent theoretical fluid dynamics studies of flapping-wing flight have shown that wing trajectories with nonzero deviation may be more efficient in terms of the power (Berman and Wang, 2007). Since real autonomous flights of current flapping wing MAVs are limited by the energy sustain, any improvement in power consumption is of vital important. Thus, the starting point of this study is to explore a potential mechanism that has capability of generating complex wing trajectories.

1.2 Flight Muscles

To figure out how different wing trajectories are generated in insects, it is necessary to understand the physical structure and the functionality of their flight muscles first. Many flying insects employ two types of muscles: synchronous and asynchronous (Dudley, R., 1999). Here, we will review the physical structure and functionality of each group.

As the naming suggests, each contraction of synchronous flight muscle is synchronized with the action of nerve impulse, as is the case in vertebrate skeletal muscle (Dudley, R., 1999). These muscles are placed vertically to the long axis of the insects, as shown in Figure 1.2(1). One attached to the wing is called elevator muscle, and the other attached to the floor of the thorax structure is called depressor muscle (Hill *et al.* 2012). Contraction of the elevator muscles raises the wings, and contraction of the depressor muscles drives the wing down. Synchronous flight muscles are found in some insects,

such as locusts and dragonflies, which usually flap at a relative low frequency with a large wing (Dudley, R., 1999).

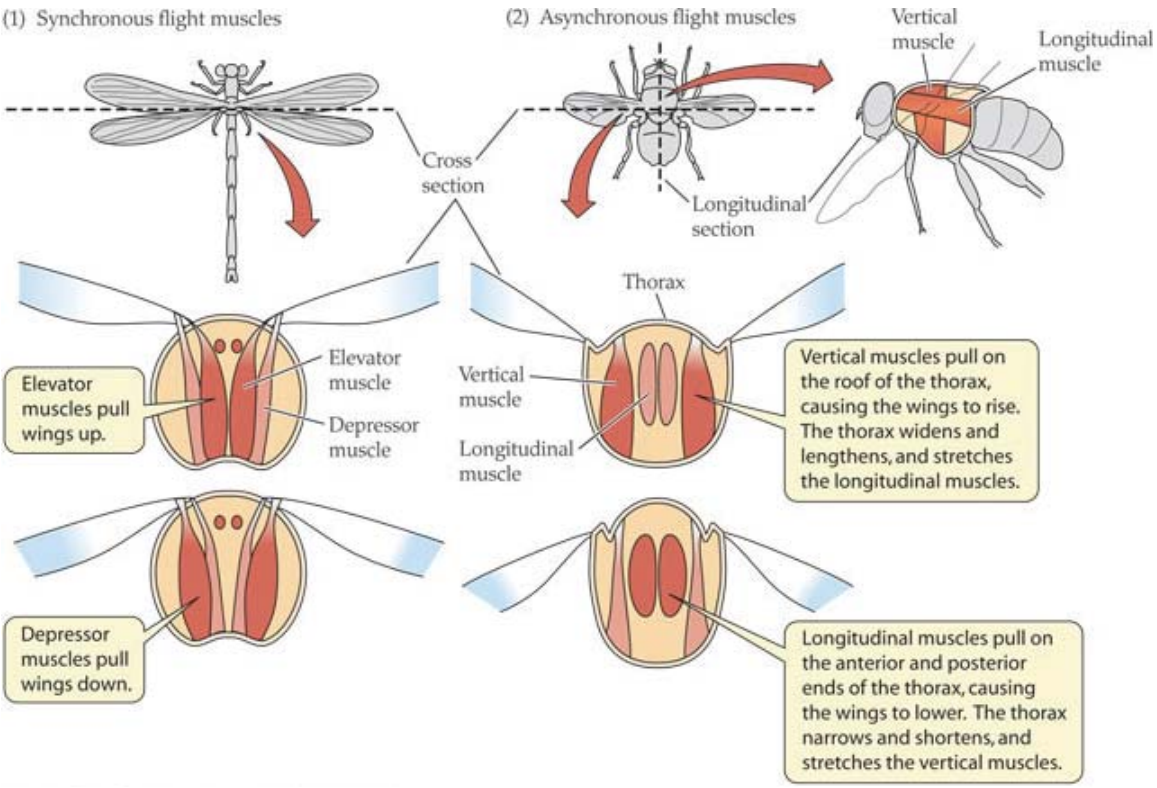

Figure 1.2. Synchronous and asynchronous flight muscles. (1) The cross section of the flight muscle of a dragonfly is portrayed. Synchronous flight muscles attach directly to the wing. (2) The cross section and longitudinal section of the flight muscle of a housefly are portrayed. Asynchronous flight muscles attach to the thorax and are arranged perpendicular to each other. Contractions of muscles are in red color, and relaxed muscles are in pink. Adapt from (Hill *et al.* 2012).

Some insects including flies, bees, and beetles not only use synchronous flight muscles, but also use asynchronous flight muscles, of which contractions are not synchronized with the nerve impulse. Asynchronous flight muscles are not directly attached to the wings, and are primarily responsible for power generation. The mechanical energy from asynchronous flight muscles is to excite a resonant flapping

motion through a transmission system connecting the thorax and the wing hinge. Asynchronous muscles are also called as power muscles. When operating against inertial load of the air moved by the wings, these muscles act as a self-sustaining oscillator that may execute several stroke cycles for every electrical stimulus received (McMahon, 1984). Additionally, these muscles can act as springs that conserve the kinetic energy during flapping, and were considered to increase the power efficiencies (Tu and Dickinson, 1994; Dickinson and Lighton, 1995). Figure 1.2(2) shows the generalized morphology of power muscle in housefly. Two opposing pairs of power muscles are attached to the thorax structure rather than the wings, with one placed vertically and the other longitudinally. Contraction of the vertical muscles pull down on the roof of the thorax and deform its sides, causing the wings to move up through the transmission system. When the longitudinal depressor muscles contract, the roof of the thorax bulges up, resulting to move the wings down (Hill *et al.* 2012).

On the other hand, synchronous flight muscles in these insects, also called as controller muscles, act as a transmission system that determines how the mechanical energy produced by the power muscles is transformed into wing motion (Tu and Dickinson, 1997). The mechanism of the transmission system is really complex. Biologists found that there were 18 pairs of small muscles that were responsible for the fine control of wing motion (Williams and Williams, 1943; Wisser and Nachtigall, 1984; Tu and Dickinson, 1997). Among these controller muscles, only small parts were identified their roles. Tu and Dickinson (1996) conducted experiments on blowflies using high speed videography techniques and electromyograms to record the wing kinematics and muscle activation signals simultaneously. It was found that the blowfly changed its

wing trajectory from a figure-of-eight pattern when the first and second basalare control muscles were inactive, to an oval shape pattern, when these muscles were activated, as shown in Figure 1.3. Changes in activation phase tuned the stiffness of muscle, resulting in the alteration of the wing trajectory.

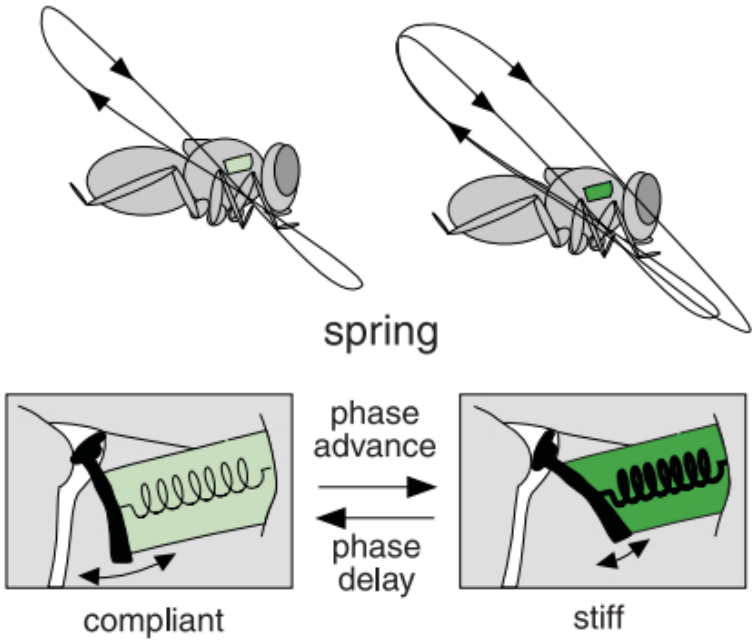

Figure 1.3. Controller muscles acts to steer and direct the power produced by the power flight muscles. Adapted from (Tu and Dickinson, 1996).

1.3 Scope and Outline of Thesis

In this study, we investigate simple and effective mechanisms of flight muscle that are potentially used in real insects, thereby providing inspiration for flapping wing MAVs design. The remainder of the thesis is organized as followers. Chapter 2 presents the mechanism of a flapping wing oscillation system, as well as models of insect flight muscles. Using a blade-element model and a quasi-steady model, a dynamic model is

then developed. In Chapter 3, we use these models to explain how different wing trajectories are generated by the interaction between aerodynamic moments and elastic moments of the system. Chapter 4 presents a hybrid optimization algorithm combining aspects of a genetic algorithm and a Nelder-Mead simplex algorithm. With this algorithm, we find the optimal wing kinematics that maximizes the power efficiency while still providing enough lift to fly. Finally, Chapter 5 concludes this work.

CHAPTER 2. DYNAMIC MODELING OF FLAPPING WINGS

In this chapter, we describe the mechanism of a flapping wing oscillation system, as well as mathematical models for calculating forces, torques, and power consumption.

2.1 Coordinate Definitions

We assume that an insect's wing is a rigid plate and is allowed to rotate through each of its three Euler angles: the stroke angle ϕ, the rotation angle ψ and the deviation angle θ. Figure 2.1 shows coordinate systems and Euler angles for a basis description of the rigid wing kinematics. Upstroke is the ventral-to-dorsal motion of the flapping wing, and downstroke is the dorsal-to-ventral motion. A left wing is shown at its downstroke. *OXYZ* is a body-fix coordinate system. *oxyz* is a frame fixed on the wing. They share the same origin *O* that is the base of the wing. We assume that the insect body is vertical. We define *Z* is the vertical direction, *X* is the forward direction of the insect, and *Y* is the perpendicular to the forward direction in the horizontal plane. *XY* plane is called the stroke plane of the wing. *y* is along the leading edge of the wing and the positive direction is defined from the root of the wing to the wing tip. The positive *z* -axis is along the wing chord and from the trailing edge to the leading edge. Finally, *x* -axis is defined by the right-hand rule. First, the $x''y''z''$ -axes rotate with the stroke angle ϕ. The axis of rotation is the positive *Z* -axis, and ϕ is defined as either the angle between the y'' -axis

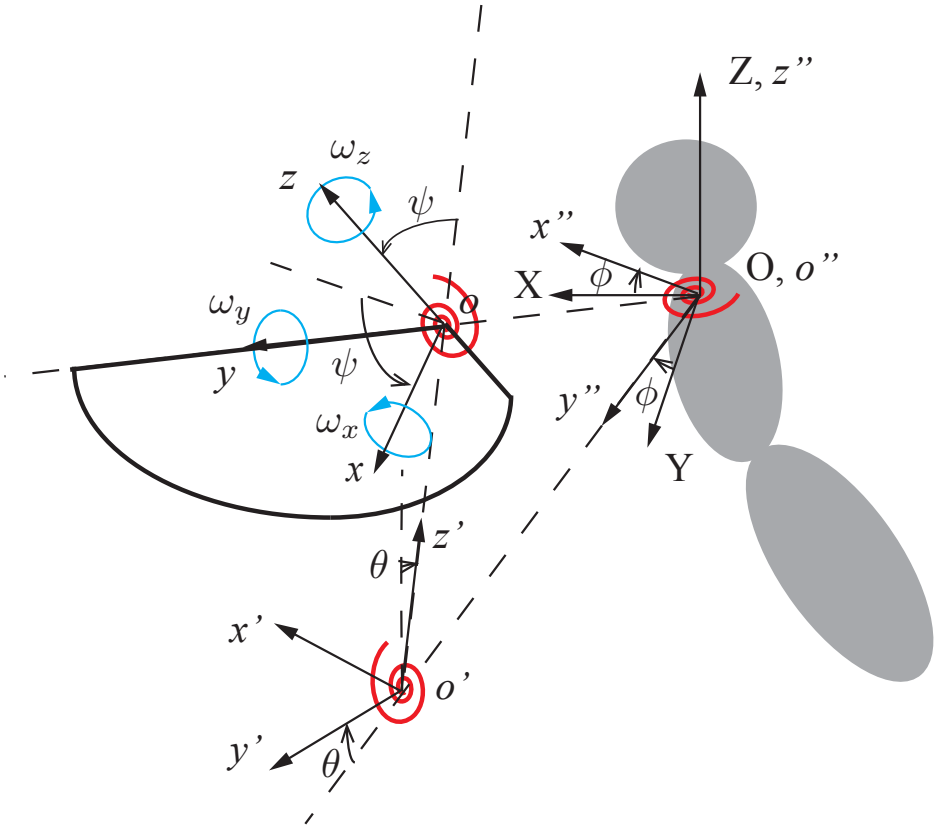

Figure 2.1. Coordinate systems and Euler angles, shown for a left wing and vertical-body orientation. All origins of the coordinate systems share the same point, O. They are shown offset only for charity. Local angular velocities ω_x, ω_y and ω_z are plotted in light blue. Spirals in red represent flight muscles at each Euler angle, which will be discussed in Section 2.2.

and the Y-axis or the angle between the x''-axis and the X-axis. ϕ is zero where the wing is at its mid-stroke position. In Figure 2.1, ϕ is shown with a negative value. Then, the $x'y'z'$-axes rotate with the deviation angle θ, defined as either the angle between the y''-axis and the y'-axis or the angle between the z''-axis and the z'-axis, where the

axis of rotation is x' -axis. θ is zero where the leading edge of the wing is at the stroke plane. Finally, the xyz -axes rotate with the rotation angle ψ . ψ is defined as either the angle between the x -axis and the x' -axis or the angle between the z -axis and the z' -axis, rotating about the y -axis. The coordinate systems in Figure 2.1 correspond to positive values of ϕ and ψ . The resultant eulerian rotation matrix is

$$R_{bw} = R_Z(\phi) R_X(\theta) R_Y(\psi), \tag{2.1}$$

where

$$R_Z(\phi) = \begin{bmatrix} cos\phi & -sin\phi & 0 \\ sin\phi & cos\phi & 0 \\ 0 & 0 & 1 \end{bmatrix}, \tag{2.2}$$

$$R_X(\theta) = \begin{bmatrix} 1 & 0 & 0 \\ 0 & cos\theta & -sin\theta \\ 0 & sin\theta & cos\theta \end{bmatrix}, \tag{2.3}$$

$$R_Y(\psi) = \begin{bmatrix} cos\psi & 0 & sin\psi \\ 0 & 1 & 0 \\ -sin\psi & 0 & cos\psi \end{bmatrix}. \tag{2.4}$$

The wing motion is the sum of three rotational motions along each Euler angle. The angular velocity of the wing is given by

$$\boldsymbol{\omega} = \dot{\phi}\, \boldsymbol{e}_{z''} + \dot{\theta}\, \boldsymbol{e}_{x'} + \dot{\psi}\, \boldsymbol{e}_{y}, \tag{2.5}$$

where $\boldsymbol{e}_{z''}$, $\boldsymbol{e}_{x'}$, and $\boldsymbol{e}_{y''}$ are denoted as the unit vectors along z'' –axis, x' -axis, and y –axis. $\boldsymbol{e}_x$, $\boldsymbol{e}_y$, and $\boldsymbol{e}_z$ are denoted as the unit vectors of the wing-fixed coordinate system *oxyz*. In the wing-fixed coordinate system *oxyz*, it becomes

$$\boldsymbol{\omega} = \omega_x \boldsymbol{e}_x + \omega_y \boldsymbol{e}_y + \omega_z \boldsymbol{e}_z , \tag{2.6}$$

where

$$\omega_x = -\dot{\phi}\, cos\theta\, sin\psi + \dot{\theta}\, cos\psi , \tag{2.7}$$

$$\omega_y = \dot{\phi}\, sin\theta + \dot{\psi} , \tag{2.8}$$

$$\omega_z = \dot{\phi}\, cos\theta\, cos\psi + \dot{\theta}\, sin\psi . \tag{2.9}$$

2.2 Model of Flight Muscles

As discussed in the previous section, there are two physiologically and functionally different classes of flight muscles: power muscles and control muscles (Dickinson and Tu, 1997). We model the power muscles as one actuator and one torsional spring at the stroke angle. The actuator provides a high level of mechanical energy required to drive the wing. The control muscles are modeled as two torsional springs at the rotation angle and at the deviation angle respectively. Overall, it is a three degree-of-freedom (DOF) system, consisting of one actuator and three torsional springs.

We model the input torque $\boldsymbol{M}_{input}$ as a sinusoidal form. It can be written as

$$\boldsymbol{M}_{input}(t) = M_{max} cos(2\pi f\, t)\boldsymbol{e}_{z''} , \tag{2.10}$$

where f is the driving frequency. Three torsional springs are attached to each Euler angle, as shown in Figure 2.3. $\boldsymbol{M}_{\phi,spring}$, $\boldsymbol{M}_{\theta,spring}$ and $\boldsymbol{M}_{\psi,spring}$ are denoted as the elastic torques of the stroke angle ϕ, the deviation angle θ and the rotation ψ. They are given by

$$\boldsymbol{M}_{\phi,spring} = k_\theta \theta\, \boldsymbol{e}_{x'} , \tag{2.11}$$

$$\boldsymbol{M}_{\theta,spring} = k_\theta \theta \, \boldsymbol{e}_{x'} , \tag{2.12}$$

$$\boldsymbol{M}_{\psi,spring} = k_\psi \psi \, \boldsymbol{e}_{y} . \tag{2.13}$$

where k_ϕ, k_θ, and k_ψ are stiffness value of torsional springs of ϕ, θ and ψ. Therefore, the total torque of torsional springs is

$$\boldsymbol{M}_{spring} = \boldsymbol{M}_{\phi,spring} + \boldsymbol{M}_{\theta,spring} + \boldsymbol{M}_{\psi,spring} . \tag{2.14}$$

2.3 Wing Morphology

Wing dynamics characteristics have a strong dependence on the detailed shape mass distribution of a wing. A concise mathematical description of the wing is necessary. The commonly used definitions in (Ellington, 1984a) provide a method of parameterizing a wing using key dimensional components integral to the wing. Figure 2.2 illustrates a wing platform.

The dimensionless spanwise distance from the root is

$$\hat{r} = \frac{r}{R}, \tag{2.15}$$

where *R* is the wing's base-to-tip length. The chord profile is

$$\hat{c}\left(\hat{r}\right) = \frac{c\left(r\right)}{\overline{c}} . \tag{2.16}$$

where $\overline{c}$ is the mean chord, that is defined as the area of wing divided by the wing length. Radius of *k*th moments of wing area is defined as

$$\hat{r}_k^k = \int_0^1 \hat{c}\left(\hat{r}\right) \hat{r}^k d\hat{r} . \tag{2.17}$$

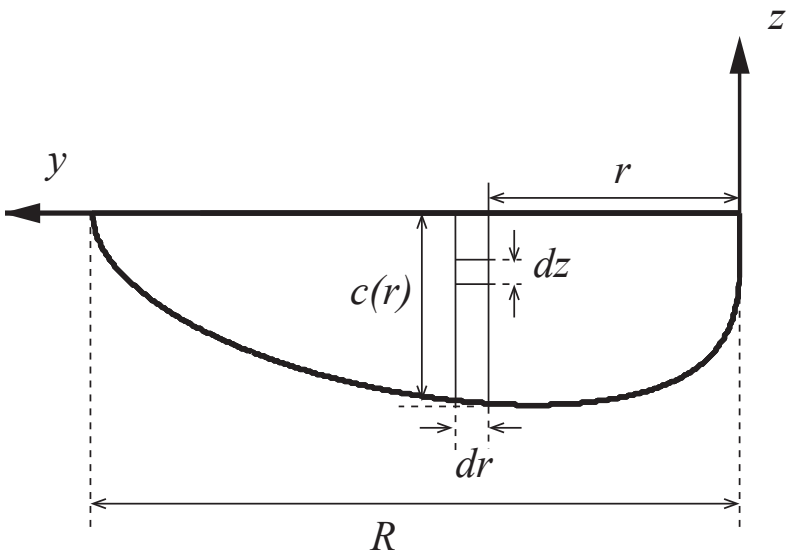

Figure 2.2. Wing platform morphological parameters. Differential elements for spacewise and chordwise integration are shown.

The higher moments can simply be expressed as function of the position of the centroid (Ellington, 1984a):

$$\hat{r}_2 = 0.929\left(\hat{r}_1\right)^{0.732} \tag{2.18}$$

and

$$\hat{r}_3 = 0.900\left(\hat{r}_1\right)^{0.581}. \tag{2.19}$$

Given only $\hat{r}_1$, the entire shape of a wing is defined by the Beta distribution as

$$c\left(\hat{r}\right) = \frac{\hat{r}^{p-1}\left(1-\hat{r}\right)^{q-1}}{B\left(p,q\right)}, \tag{2.20}$$

where the Beta distribution $B\left(p,q\right)$, p and q are

$$B\left(p,q\right) = \int_0^1 \hat{r}^{p-1}\left(1-\hat{r}\right)^{q-1} d\hat{r}, \tag{2.21}$$

$$p = \hat{r}_1\left[\frac{\hat{r}_1\left(1-\hat{r}_1\right)}{\hat{r}_2^2-\hat{r}_1^2}-1\right], \tag{2.22}$$

$$q = \left(1-\hat{r}_1\right)\left[\frac{\hat{r}_1\left(1-\hat{r}_1\right)}{\hat{r}_2^2-\hat{r}_1^2}-1\right]. \tag{2.23}$$

We assume that the wing mass is uniformly distributed over the wing platform. The mass density of the wing is 1200 $\mathrm{kg\,m^{-3}}$, and the thickness of the wing is 4.5×10^{-4} mm (Wainwright *et al*., 1982; Combes and Daniel, 2003). As the thickness of the wing is very small, the moments and products of inertia of the mass of a wing, respect to the wing-fixed coordinate system *oxyz*, is given by

$$\boldsymbol{I} = \begin{bmatrix} I_{xx} & I_{xy} & I_{xz} \\ I_{yx} & I_{yy} & I_{yz} \\ I_{zx} & I_{zy} & I_{zz} \end{bmatrix}, \tag{2.24}$$

where

$$I_{xx} = \rho_w h\iint\left(y^2+z^2\right)dydz\,, \tag{2.25}$$

$$I_{yy} = \rho_w h\iint\left(x^2+z^2\right)dxdz \approx \rho_w h\iint z^2dxdz\,, \tag{2.26}$$

$$I_{zz} = \rho_w h\iint\left(x^2+y^2\right)dxdy \approx \rho_w h\iint y^2dxdy\,, \tag{2.27}$$

$$I_{xy} = I_{yx} = -\rho_w h\iint xy\,dxdy \approx 0\,, \tag{2.28}$$

$$I_{yz} = I_{zy} = -\rho_w h\iint yz\,dydz\,, \tag{2.29}$$

$$I_{xz} = I_{zx} = -\rho_w h\iint xz\,dxdz \approx 0\,. \tag{2.30}$$

The details of morphological parameters are list in Table 2.1.

Table 2.1. Morphological parameters used for simulation.

Symbol	Description	Value
R	wing length	3 mm
AR	aspect ratio	6.19 mm
$\overline{c}$	mean chord length	0.97 mm
h	wing thickness	4.5×10^{-4} mm
ρ_w	wing mass density	1200 kg m^{-3}
$\hat{r}_1$	radius of 1st moments of wing area	0.4500
$\hat{r}_2$	radius of 2nd moments of wing area	0.5178
m_w	wing mass	1.6×10^{-6} g
I_{xx}	moment of inertia of the wing about the x axes	6.77×10^{-6} g mm^2
I_{yy}	moment of inertia of the wing about the y axes	9.53×10^{-7} g mm^2
I_{zz}	moment of inertia of the wing about the z axes	5.82×10^{-6} g mm^2
I_{yz}	product of inertia of the wing	1.64×10^{-6} g mm^2

2.4 Blade-Element Model

Blade-element model assumes that the total instantaneous force on a wing can be computed as the sum of forces acting on a set of infinitesimal chordwise strips. The forces can be calculated using the quasi-steady aerodynamic model derived from dynamically scaled flapping robots (Dickinson *et al.*, 1999). Since the quasi-steady

aerodynamic model assumes the aerodynamic performance is independent before and after the instant, wing-wing interactions (Weis-Fogh, 1973), wing capture effects (Dickinson *et al.*, 1999) and other unsteady phenomena are not included. Another approach for calculation of forces on wings is computational fluid dynamics (CFD) (Mao and Tang, 2002a). By solving three-dimensional incompressible unsteady Navier-Stokes equations numerically, CFD gets the solution of unsteady aerodynamic forces. However, CFD is computationally costly and can only be carried out with known wing kinematics. The chief advantage of blade-element model is its simplicity and rapid computation. It captures the primary dynamic properties of the system, and provides a feasible method to perform studies that require a large number of evaluations of some flight characteristic. Therefore it is widely used in parameters studies, such as flight control (Hedrick and Daniel, 2006), energy minimization (Berman and Wang, 2007) and preliminary design of flapping-wing micro air vehicle (Cheng, *et al*. 2013).

In blade-element model, the instantaneous forces generated by a thin, flapping wing may be represented as the sum of four force components:

$$\boldsymbol{F}_{aero} = \boldsymbol{F}_{tran} + \boldsymbol{F}_{rot} + \boldsymbol{F}_{am} + \boldsymbol{F}_{wc}, \tag{2.31}$$

where $\boldsymbol{F}_{tran}$ is the translational force, $\boldsymbol{F}_{rot}$ is the rotational force, $\boldsymbol{F}_{am}$ is the force due to the inertia of the added mass of the fluid, and $\boldsymbol{F}_{wc}$ is the force created by wake capture. Translational force estimates are quasi-steady approximations adapted from thin airfoil theory (Dickinson, *et al*., 1999.). Rotational lift can be explained in terms of the added air circulation induced by the rotation of the wing around its axis (Sane and Dickinson, 2002.). The added air mass force is generated by the inertia of the airflow generated by

unsteady wing motion. As the wing translates, it generates airflow in the same direction and any change in the wing's motion causes the airflow to impart a moment on it thereby inducing rotation (Sedov, 1965.). This force is hard to approximate analytically in three-dimensional fashion, therefore it is omitted from the dynamical model. The wake capture effect is an unsteady phenomenon occurring when the wing traverses vortices and air circulation generated by its motion prior to the direction change. As the wake capture effect cannot be modeled using the quasi-steady aerodynamic model, this force is not included in any calculations below. It should be noted that the obtained results from quasi-steady aerodynamic model are underestimated. In the following calculation, we consider two force components estimated from quasi-static aerodynamic model, and Equation 2.31 is simplified to:

$$\boldsymbol{F}_{aero} = \boldsymbol{F}_{tran} + \boldsymbol{F}_{rot}\,. \tag{2.32}$$

Aerodynamic forces and moments acting on a wing section are functions of local wing velocity and local angle of attack (AoA) α. The local wing velocity is (ignore the spanwise velocity)

$$\boldsymbol{v}_{local} = \left(\omega_x \boldsymbol{e}_x + \omega_z \boldsymbol{e}_z\right) \times r\, \boldsymbol{e}_y = -r\, \omega_z \boldsymbol{e}_x + r\, \omega_x \boldsymbol{e}_z\,. \tag{2.33}$$

Components of the local wing velocity along *x* direction and *z* direction can be written as

$$v_x\left(r\right) = -r\omega_z \tag{2.34}$$

and

$$v_z\left(r\right) = r\omega_x\,. \tag{2.35}$$

Local angle of attack α is defined as the angle between the wing chord and the direction of local velocity (Figure 2.3), which is given by

$$\alpha = \begin{cases} \frac{\pi}{2} - \beta & v_x(r) > 0 \text{ and } v_z(r) > 0 \\ -\frac{\pi}{2} + \beta & v_x(r) < 0 \text{ and } v_z(r) > 0 \\ \frac{3\pi}{2} + \beta & v_x(r) < 0 \text{ and } v_z(r) < 0 \\ \frac{\pi}{2} - \beta & v_x(r) > 0 \text{ and } v_z(r) < 0 \end{cases}, \tag{2.36}$$

where

$$\beta = atan2\left[v_z(r), v_x(r)\right]. \tag{2.37}$$

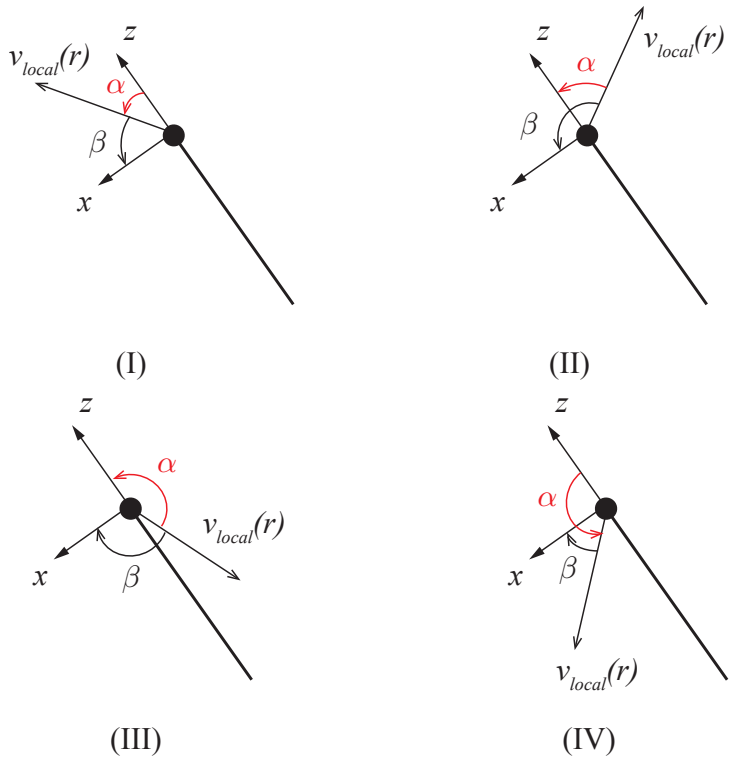

Figure 2.3. An illustration of wing's local angle of attack. Wing cross sections are portrayed. These lines represent the wing chord, and the dots represent the leading edges. Four different cases of local angle of attack are shown. Case (I) is $v_x(r) > 0$ and $v_z(r) > 0$. Case (II) is $v_x(r) < 0$ and $v_z(r) > 0$. Case (III) is $v_x(r) < 0$ and $v_z(r) < 0$. Case (IV) is $v_x(r) > 0$ and $v_z(r) < 0$.

2.4.1 Translational Force

The local translational force $d\boldsymbol{F}_{tran}(r)$ acting on a wing section at spanwise location r is decomposed into drag and lift components, which is given by

$$d\boldsymbol{F}_{tran}(r) = d\boldsymbol{F}_{D}(r) + d\boldsymbol{F}_{L}(r), \tag{2.38}$$

where $d\boldsymbol{F}_{D}(r)$ and $d\boldsymbol{F}_{L}(r)$ are drag and lift components. We denote $\boldsymbol{e}_{tran}(r)$ as the unit vector of the direction of the translational force. The drag is defined along the opposite direction of the local wing velocity, and the direction of the lift is orthogonal, as shown in Figure 2.4. The unit vector of the direction of drag can be written as

$$\boldsymbol{e}_{D}(r) = -\frac{\boldsymbol{v}_{local}(r)}{\left\|\boldsymbol{v}_{local}(r)\right\|}. \tag{2.39}$$

The unit vector of the direction of lift is

$$\boldsymbol{e}_{L}(r) = -R_{y}(\gamma)\frac{\boldsymbol{v}_{local}(r)}{\left\|\boldsymbol{v}_{local}(r)\right\|}, \tag{2.40}$$

where

$$\gamma = \begin{cases} -\dfrac{\pi}{2} & v_{x}(r) > 0 \\ \dfrac{\pi}{2} & v_{x}(r) < 0 \end{cases}. \tag{2.41}$$

Next, the drag and the lift are given by (Dickinson *et al.*, 1999):

$$d\boldsymbol{F}_{D}(r) = \frac{1}{2}C_{D}(\alpha)\rho_{air}c(r)dr\left\|v_{local}(r)\right\|^{2}\boldsymbol{e}_{D}(r) \tag{2.42}$$

$$= \frac{1}{2}C_{D}(\alpha)\rho_{air}c(r)r^{2}dr\left(\omega_{x}^{2}+\omega_{z}^{2}\right)\boldsymbol{e}_{D}(r), \tag{2.43}$$

$$d\boldsymbol{F}_L(r) = \frac{1}{2} C_L(\alpha) \rho_{air} c(r) dr \left\| v_{local}(r) \right\|^2 \boldsymbol{e}_L(r) \tag{2.44}$$

$$= \frac{1}{2} C_L(\alpha) \rho_{air} c(r) r^2 dr \left(\omega_x^2 + \omega_z^2 \right) \boldsymbol{e}_L(r), \tag{2.45}$$

(A)

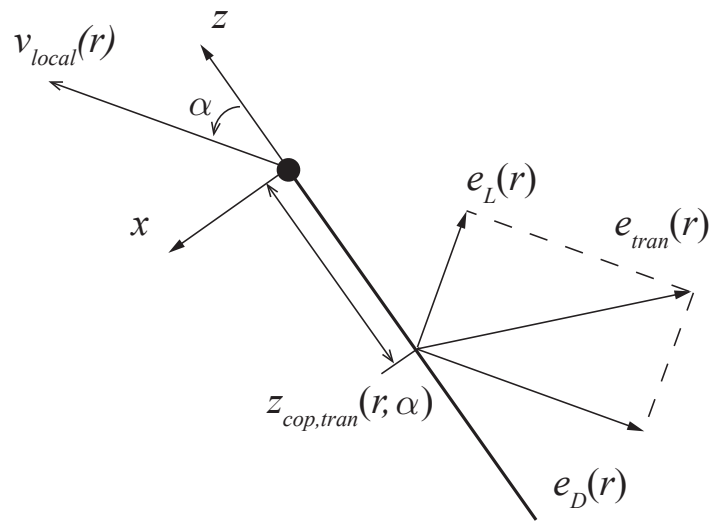

(B)

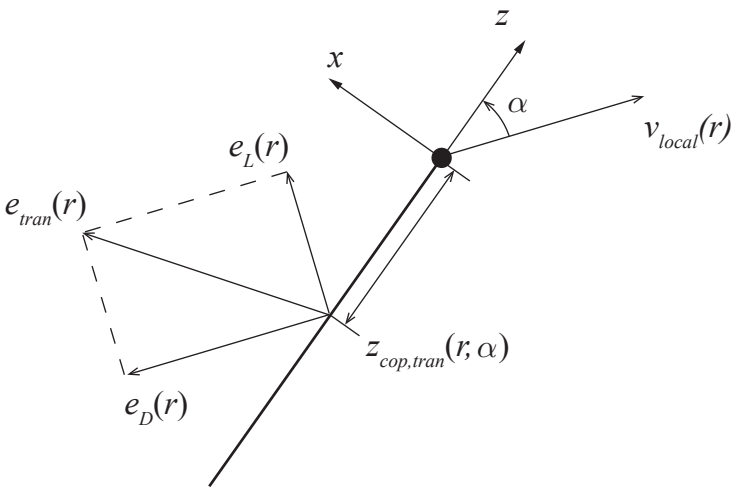

Figure 2.4. An illustration of translational forces. Wing cross sections are portrayed. These lines represent the wing chord, and the dots represent the leading edges. Case (A) is $v_x(r) > 0$. Case (B) is $v_x(r) < 0$.

where ρ_{air} is the air density, that is $1.23\times10^{-6}\,\mathrm{g\,mm^{-6}}$, and $C_D(\alpha)$ and $C_L(\alpha)$ are the translational lift and drag coefficients, respectively. Their expressions are given by (Dickinson, *et al*., 1999):

$$C_D(\alpha) = 0.225 + 1.58 sin(2.13\alpha - 7.2), \tag{2.46}$$

$$C_L(\alpha) = 1.92 - 1.55 cos(2.04\alpha - 9.82), \tag{2.47}$$

where α is in degree. Integrating these chordwise strips results in the translational force for the wing:

$$\boldsymbol{F}_{tran} = \int_0^R \left[d\boldsymbol{F}_D(r) + d\boldsymbol{F}_L(r) \right]. \tag{2.48}$$

The location of the center of pressure of $d\boldsymbol{F}_D(r)$ and $d\boldsymbol{F}_L(r)$ at each wing section is

$$\boldsymbol{r}_{cop,tran}(r,\alpha) = r\boldsymbol{e}_y - z_{cop,tran}(r,\alpha)\boldsymbol{e}_z, \tag{2.49}$$

where α is in degree, and $z_{cop,tran}$ is the chordwise location of center of pressure (Dickson, *et al*., 2006). It is given by:

$$z_{cop,tran}(r,\alpha) = c(r)\hat{d}_{cop}(\alpha) \tag{2.50}$$

and

$$\hat{d}_{cop}(\alpha) = \frac{0.82}{\pi}|\alpha| + 0.05. \tag{2.51}$$

Then, drag and lift aerodynamic moments are given by:

$$d\boldsymbol{M}_D(r) = \boldsymbol{r}_{cop,tran}(r,\alpha) \times d\boldsymbol{F}_D(r) \tag{2.52}$$

and

$$d\boldsymbol{M}_L(r) = \boldsymbol{r}_{cop,tran}(r,\alpha) \times d\boldsymbol{F}_L(r). \tag{2.53}$$

Integrating Equation 2.52 and Equation 2.53 lead to

$$\boldsymbol{M}_D(r) = \int_0^R d\boldsymbol{M}_D(r) = \int_0^R \boldsymbol{r}_{cop,tran}(r,\alpha) \times d\boldsymbol{F}_D(r) \tag{2.54}$$

and

$$\boldsymbol{M}_L(r) = \int_0^R d\boldsymbol{M}_L(r) = \int_0^R \boldsymbol{r}_{cop,tran}(r,\alpha) \times d\boldsymbol{F}_L(r). \tag{2.55}$$

Finally the translational moment is

$$\boldsymbol{M}_{tran} = \boldsymbol{M}_D + \boldsymbol{M}_L. \tag{2.56}$$

2.4.2 Rotational Force

The model for rotational forces is that of a thin wing flapping at low α, with the rotational forces arising from a coupling of translation and rotation. Experiments (Sane and Dickinson, 2002) have shown that the rotational force is a function of the instantaneous rotation rate and the location of the rotational axis. The rotational force on the wing has the form

$$dF_{rot} = C_{rot}\rho_{air} \left\| \boldsymbol{v}_{local}(r) \right\| \left| \omega_y \right| c(r)^2 \, dr, \tag{2.57}$$

where C_{rot} is the rotational coefficient. Its expression is given by (Sane and Dickinson, 2002):

$$C_{rot} = \pi\left(0.75 - \hat{z}_0\right), \tag{2.58}$$

where $\hat{z}_0$ is a non-dimensional term defined by the position of the axis of rotation. The leading edge corresponds to a value of 0, whereas the trailing edge corresponds to a value of 1. A value of 0.75 represents the critical axis around which the wing generates no force

as it rotates. In our model, the rotational axis is along the leading edge, and $\hat{z}_0 = 0$. The rotational force acts perpendicular to the wing surface. The direction of the unit vector of the rotational force is illustrated in Figure 2.5, and it has the form:

$$\boldsymbol{e}_{rot} = sign\left(\omega_y\right)\boldsymbol{e}_x . \tag{2.59}$$

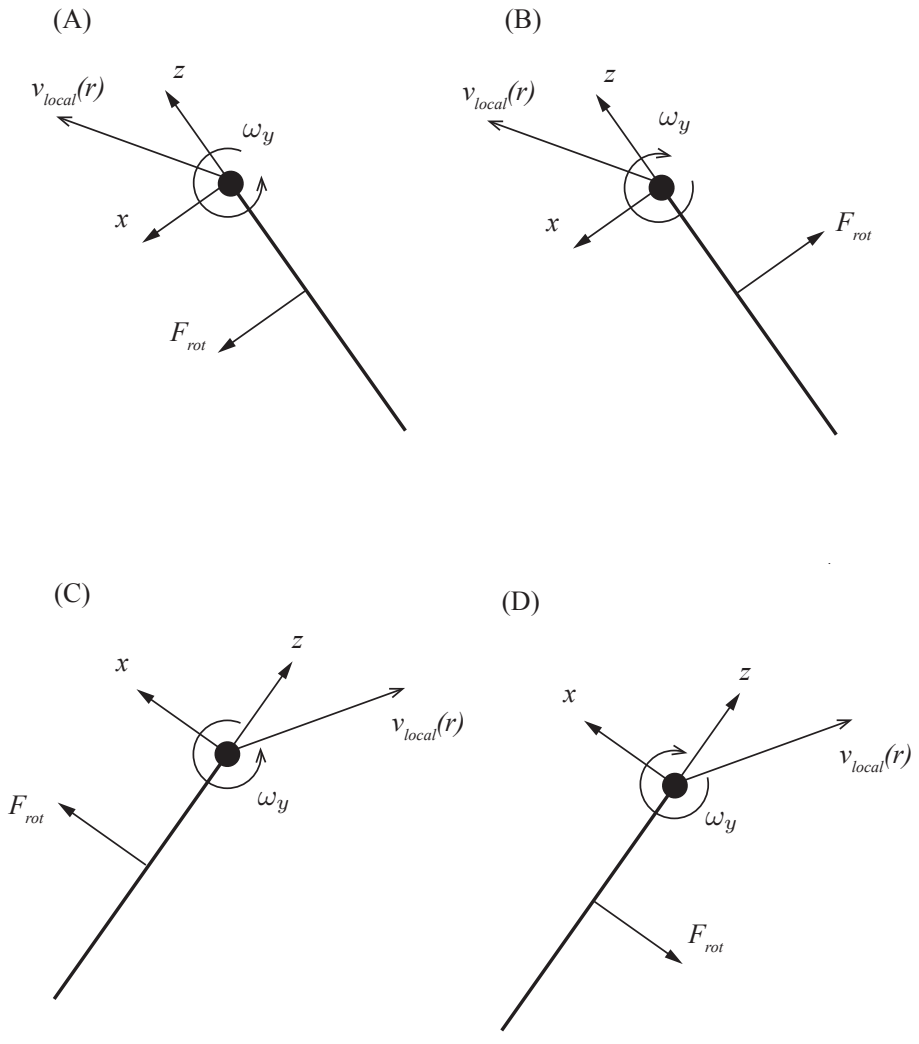

Figure 2.5. An illustration of rotational forces. Wing cross sections are portrayed. These lines represent the wing chord, and the dots represent the leading edges.

Finally, the rotational force is given by

$$dF_{rot} = C_{rot}\rho_{air}\left\|\boldsymbol{v}_{local}(r)\right\|\left|\omega_y\right|\bar{c}^2 R\int_0^1 \hat{r}\hat{c}\left(\hat{r}\right)^2 d\hat{r}\,\boldsymbol{e}_{rot}. \tag{2.60}$$

The rotational force, describe previously, is included in the calculation of aerodynamic forces, but not included in the calculation of aerodynamic moments. The primary reason is that there are no direct measurements of the center of pressure of these rotational forces. The prediction of rotational moment could not be realized. Future investigations are needed for calculation of the center of pressure of these rotational forces.

2.4.3 Rotational Damping Moment

Whitney and Wood (2010) have found that the translational and rotational aerodynamic forces failed to predict a rotational damping moment exerted on the wing. To calculate this moment, the relative velocity due to rotation of the wing is considered. The relative air velocity is zero at the rotational axis that is along the leading edge, and increases away from it, as shown in Figure 2.6. The rotational damping force has the form:

$$d^2\boldsymbol{F}_{rd}(r,z) = -\frac{1}{2}C_{rd}\rho_{air}\left|\omega_y\right|\omega_y dr\left|z\right|z\,dz\,\boldsymbol{e}_x, \tag{2.61}$$

where C_{rd} is the rotational damping force coefficient. Andersen *et al*. (2005) used a value of 2, because this is the theoretical result of rotational drag on a flat plate subjected to normal flow. This value here is taken to be 5, as experiments (Whitney and Wood, 2010)

demonstrate that this value led to the best agreement between measured and predicted passive-rotation trajectories.

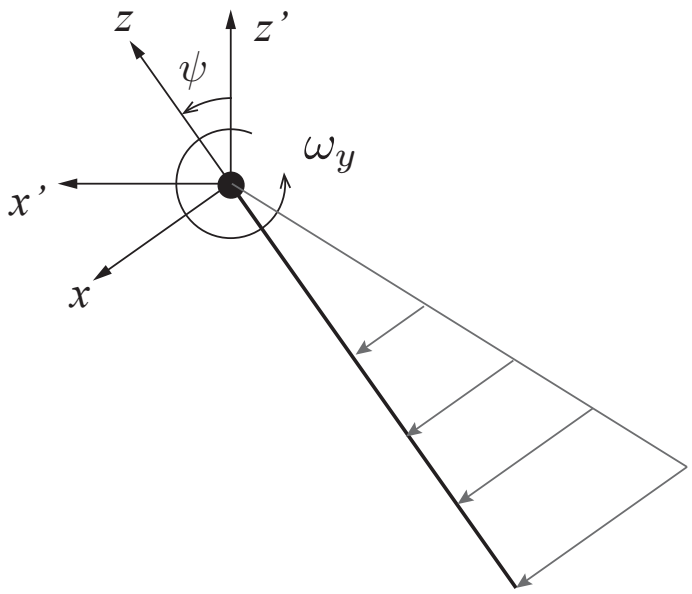

Figure 2.6. Relative velocity profile by the pure rotation of the wing. Wing cross sections are portrayed. These lines represent the wing chord, and the dots represent the leading edges.

The acting point of the rotational damping force is

$$\boldsymbol{r}_{rot}\left(r\right)=r\boldsymbol{e}_{y}+z\boldsymbol{e}_{z}. \tag{2.62}$$

We then have the rotational damping moment:

$$d^{2}\boldsymbol{M}_{rd}\left(r,z\right)=\boldsymbol{r}_{rot}\left(r\right)\times d^{2}\boldsymbol{F}_{rd}\left(r,z\right). \tag{2.63}$$

Integrating Equation 2.63 leads to

$$\boldsymbol{M}_{rd}=\int_{0}^{R}\int_{-c(r)}^{0}\boldsymbol{r}_{rot}\left(r\right)\times d^{2}\boldsymbol{F}_{rd}\left(r,z\right)=M_{rd}^{y}\boldsymbol{e}_{y}+M_{rd}^{z}\boldsymbol{e}_{z}. \tag{2.64}$$

2.5 Equation of Motion

The insect wing is modeled as a rigid body with three Euler angle. In the wing-fixed coordinate system *oxyz*, the equations of motion of the wing can be written as

$$\boldsymbol{I}\cdot\dot{\boldsymbol{\omega}}+\boldsymbol{\omega}\times\boldsymbol{I}\cdot\boldsymbol{\omega}=\boldsymbol{M}_{aero}+\boldsymbol{M}_{gravity}+\boldsymbol{M}_{spring}+\boldsymbol{M}_{input}, \tag{2.65}$$

where the first term and the second term $\boldsymbol{I}\cdot\dot{\boldsymbol{\omega}}+\boldsymbol{\omega}\times\boldsymbol{I}\bullet\omega$ are the inertial moment. The aerodynamic moment $\boldsymbol{M}_{aero}$ is given by

$$\boldsymbol{M}_{aero}=\boldsymbol{M}_{tran}+\boldsymbol{M}_{rd}\,. \tag{2.66}$$

The gravity moment $\boldsymbol{M}_{gravity}$ is given by

$$\boldsymbol{M}_{gravity}=\boldsymbol{r}_g\times\boldsymbol{F}_g, \tag{2.67}$$

where $\boldsymbol{r}_g$ is denoted as the vector of center of mass in the wing-fixed coordinate system *oxyz* and $\boldsymbol{F}_g$ is denoted as the gravity. $\boldsymbol{r}_g$ is given by

$$\boldsymbol{r}_g=r_{com}\boldsymbol{e}_y-c_{com}\boldsymbol{e}_z, \tag{2.68}$$

where $r_{com}=1.5$ mm, and $c_{com}=4.85$ mm. $\boldsymbol{F}_g$ is given by

$$\boldsymbol{F}_g=m_w g\,\boldsymbol{e}_Z, \tag{2.69}$$

where g = 9.81 m/s^2.

Substituting all the know quantities into Equation 2.65, we obtain the following nonlinear ordinary differential equations (ODEs):

$$\begin{aligned}&I_{xx}\dot{\omega}_x+\left(I_{zz}-I_{yy}\right)\omega_y\omega_z+I_{yz}\left(\omega_y^2-\omega_z^2\right)=\boldsymbol{e}_x\cdot\boldsymbol{M}_{gravity}+\boldsymbol{e}_x\cdot\boldsymbol{M}_{aero}\\&+\boldsymbol{e}_x\cdot\left(k_\phi\phi\,\boldsymbol{e}_{z''}+k_\theta\theta\,\boldsymbol{e}_{x'}+k_\psi\psi\,\boldsymbol{e}_y\right)+\boldsymbol{e}_x\cdot M_{max}\cos\left(2\pi f\,t\right)\boldsymbol{e}_{z''}\,,\end{aligned} \tag{2.70}$$

$$I_{yy}\dot{\omega}_y + I_{yz}\dot{\omega}_z + \left(I_{xx} - I_{zz}\right)\omega_x\omega_z - I_{yz}\omega_x\omega_y = \boldsymbol{e}_y \cdot \boldsymbol{M}_{gravity} + \boldsymbol{e}_y \cdot \boldsymbol{M}_{aero} + \boldsymbol{e}_y \cdot \left(k_\phi \phi\, \boldsymbol{e}_{z''} + k_\theta \theta\, \boldsymbol{e}_{x'} + k_\psi \psi\, \boldsymbol{e}_y\right) + \boldsymbol{e}_y \cdot M_{max} \cos\left(2\pi f\, t\right)\boldsymbol{e}_{z''} \quad , \tag{2.71}$$

$$I_{zz}\dot{\omega}_z + I_{zy}\dot{\omega}_y + \left(I_{yy} - I_{xx}\right)\omega_x\omega_y + I_{zy}\omega_x\omega_z = \boldsymbol{e}_z \cdot \boldsymbol{M}_{gravity} + \boldsymbol{e}_z \cdot \boldsymbol{M}_{aero} + \boldsymbol{e}_z \cdot \left(k_\phi \phi\, \boldsymbol{e}_{z''} + k_\theta \theta\, \boldsymbol{e}_{x'} + k_\psi \psi\, \boldsymbol{e}_y\right) + \boldsymbol{e}_z \cdot M_{max} \cos\left(2\pi f\, t\right)\boldsymbol{e}_{z''} \quad . \tag{2.72}$$

2.6 Dimensional Analysis

After we get the equation of motion, dimensional analysis is used to reduce the number of variables and to get an insight into the possible mathematical structure of this oscillatory system. In Equation 2.65, the independent variable is time *t*, and the dependent variables are ϕ, θ and ψ. Then we replace each of them with a quantity scaled. We set

$$t = \frac{\hat{t}}{f}, \tag{2.73}$$

$$\phi = 2\pi\,\hat{\phi}, \tag{2.74}$$

$$\theta = 2\pi\,\hat{\theta}, \tag{2.75}$$

$$\psi = 2\pi\,\hat{\psi}. \tag{2.76}$$

where *f* is the driving frequency of the input torque in Equation 2.10. Equation 2.54, 2.55, 2.64 and 2.66 show

$$\boldsymbol{M}_{aero} \propto \boldsymbol{\omega}^2. \tag{2.77}$$

Substituting Equations 2.73 – 2.76 into Equations 2.70-2.72 and simplifying, we have the non-dimensional ODEs:

$$\hat{\dot{\omega}}_x + \frac{2\pi\left(I_{zz} - I_{yy}\right)}{I_{xx}}\hat{\omega}_y\hat{\omega}_z + \frac{2\pi I_{yz}}{I_{xx}}\left(\hat{\omega}_y^2 - \hat{\omega}_z^2\right)$$
$$= \frac{1}{2\pi I_{xx} f^2}\boldsymbol{e}_x \cdot \boldsymbol{M}_{gravity} + \frac{2\pi}{I_{xx}}\boldsymbol{e}_x \cdot \hat{\boldsymbol{M}}_{aero} \tag{2.78}$$
$$+ \frac{1}{I_{xx} f^2}\boldsymbol{e}_x \cdot \left(k_\phi \hat{\phi}\, \boldsymbol{e}_{z''} + k_\theta \hat{\theta}\, \boldsymbol{e}_{x'} + k_\psi \hat{\psi}\, \boldsymbol{e}_y\right) + \frac{1}{2\pi I_{xx} f^2}\boldsymbol{e}_x \cdot M_{max}\cos\left(2\pi\, \hat{t}\right)\boldsymbol{e}_{z''} \quad ,$$

$$\frac{I_{yy}}{I_{xx}}\hat{\dot{\omega}}_y + \frac{I_{yz}}{I_{xx}}\hat{\dot{\omega}}_z + \frac{2\pi\left(I_{xx} - I_{zz}\right)}{I_{xx}}\hat{\omega}_x\hat{\omega}_z - \frac{2\pi I_{yz}}{I_{xx}}\hat{\omega}_x\hat{\omega}_y =$$
$$\frac{1}{2\pi I_{xx} f^2}\boldsymbol{e}_y \cdot \boldsymbol{M}_{gravity} + \frac{2\pi}{I_{xx}}\boldsymbol{e}_y \cdot \hat{\boldsymbol{M}}_{aero} \tag{2.79}$$
$$+ \frac{1}{I_{xx} f^2}\boldsymbol{e}_y \cdot \left(k_\phi \hat{\phi}\, \boldsymbol{e}_{z''} + k_\theta \hat{\theta}\, \boldsymbol{e}_{x'} + k_\psi \hat{\psi}\, \boldsymbol{e}_y\right) + \frac{1}{2\pi I_{xx} f^2}\boldsymbol{e}_y \cdot M_{max}\cos\left(2\pi\, \hat{t}\right)\boldsymbol{e}_{z''} \quad ,$$

$$\frac{I_{zz}}{I_{xx}}\hat{\dot{\omega}}_z + \frac{I_{zy}}{I_{xx}}\hat{\dot{\omega}}_y + \frac{2\pi\left(I_{yy} - I_{xx}\right)}{I_{xx}}\hat{\omega}_x\hat{\omega}_y + \frac{2\pi I_{yz}}{I_{xx}}\hat{\omega}_x\hat{\omega}_z =$$
$$\frac{1}{2\pi I_{xx} f^2}\boldsymbol{e}_z \cdot \boldsymbol{M}_{gravity} + \frac{2\pi}{I_{xx}}\boldsymbol{e}_z \cdot \hat{\boldsymbol{M}}_{aero} \tag{2.80}$$
$$+ \frac{1}{I_{xx} f^2}\boldsymbol{e}_z \cdot \left(k_\phi \hat{\phi}\, \boldsymbol{e}_{z''} + k_\theta \hat{\theta}\, \boldsymbol{e}_{x'} + k_\psi \hat{\psi}\, \boldsymbol{e}_y\right) + \frac{1}{2\pi I_{xx} f^2}\boldsymbol{e}_z \cdot M_{max}\cos\left(2\pi\, \hat{t}\right)\boldsymbol{e}_{z''} \quad .$$

The expressions of $\hat{\boldsymbol{M}}_{aero}$ can be found in Appendix A. From Equation 2.78-2.80, four coefficients can be obtained to represent the dynamic property of the system. They are stroke stiffness coefficient, deviation stiffness coefficient, rotation stiffness coefficient and input torque coefficient, which are given by

$$\hat{k}_\phi = \frac{k_\phi}{I_{xx} f^2}\,, \tag{2.81}$$

$$\hat{k}_\theta = \frac{k_\theta}{I_{xx} f^2}\,, \tag{2.82}$$

$$\hat{k}_{\psi} = \frac{k_{\psi}}{I_{xx} f^2}, \tag{2.83}$$

$$\hat{M}_{max} = \frac{M_{max}}{2\pi I_{xx} f^2}. \tag{2.84}$$

From Equation 2.78-2.80, it can be seen that motions at Euler angles ϕ, θ and ψ are coupled. The motion at the stroke angle contributes to inertial torques at the rotation angle and at the deviation angle and *vice versa*.

2.7 Lift-to-Weight Ratio and Forces Coefficients

The total lift on the wing is calculated by transforming the aerodynamics force $\boldsymbol{F}_{aero}$ back into the inertial coordinate frame, in which $\boldsymbol{e}_z$ is the unit vector in the vertical direction. We define F_Z as the magnitude of $\boldsymbol{e}_z$ component of the total force that is given by

$$F_z = \boldsymbol{F}_{aero} \cdot \boldsymbol{e}_Z. \tag{2.85}$$

In order to make a non-dimensional measure of the vertical force on an insect, we will subsequently quantify an insect's lift by *L*, lift-to-weight ratio, which is given by

$$L = \frac{2\bar{F}_Z}{mg}, \tag{2.86}$$

where $\bar{F}_z$ is the average value of aerodynamic lift F_Z during one wingbeat, and *m* is the total weight of the insect. If $L \geq 1$, the insect is able to produce enough lift to fly. Aerodynamic forces are quantified in the similar way. Aerodynamic force coefficients are given by

$$C_{F,aero} = \frac{2\boldsymbol{F}_{aero} \cdot \boldsymbol{e}_Z}{mg}, \tag{2.87}$$

$$C_{F,tran} = \frac{2\boldsymbol{F}_{tran} \cdot \boldsymbol{e}_Z}{mg}, \tag{2.88}$$

$$C_{F,rot} = \frac{2\boldsymbol{F}_{rot} \cdot \boldsymbol{e}_Z}{mg}. \tag{2.89}$$

2.8 Hovering Efficiency

Power loading and disk loading are widely used as direct indicators of the lift thrust efficiency and the power consumption in a hovering helicopter (Leishman, 2006). Disk loading of a hovering helicopter is the ratio of its weight to the total main rotor disc area. It is determined by dividing the total helicopter weight by the rotor disc area, which is the area swept by the blades of a rotor. The disk loading can be defined as

$$DL = \frac{F_Z}{A_e}, \tag{2.90}$$

where A_e is denoted as the effective disk area. It is defined as the projected swept area of the lifting surfaces in the horizontal plane. For a flapping wing concept, the effective disk area is defined on the basis of the net swept area in the stroke plane over one complete wing stroke (Ellington, 1984b). So we have

$$A_e = \Phi R^2, \tag{2.91}$$

where Φ is the magnitude of the stroke angle during one flapping motion. The higher the disk loading, the more power needed to maintain the speed of the flapping motion. Helicopters and other rotorcraft are generally designed to hover with the lowest possible

power required (and hence lowest fuel burn) for a given gross weight, that is a high power loading is required (Leishman, 2006). The input power required to drive the wing is given by

$$P_{input} = M_{max} cos\left(2\pi f\, t\right)\dot{\phi}\,. \tag{2.92}$$

The power loading can be defined as:

$$PL = \frac{F_z}{P_{input}}\,. \tag{2.93}$$

$\overline{PL}$ is denoted as the average value of the power loading during one wing beat.

2.9 Stroke Cycle

We use stroke cycle to represent the wing's position during one wingbeat. The stroke cycle is defined as:

$$\tau = \frac{\hat{t}_n - \hat{t}_{\phi,min,n}}{\hat{t}_c}, \tag{3.1}$$

where $\hat{t}_{\phi,min,n}$ is denoted as the non-dimensional time in the *n*th wing beat when the stroke angle reach the minimum value, and $\hat{t}_n$ is the non-dimensional time ranged between $\hat{t}_{\phi,min,n}$ and $\hat{t}_{\phi,min,n+1}$. $\hat{t}_c$ is the non-dimensional period from $\hat{t}_{\phi,min,n}$ to $\hat{t}_{\phi,min,n+1}$. That is $\hat{t}_c = \hat{t}_{\phi,min,n+1} - \hat{t}_{\phi,min,n}$. The stroke cycle is less than 0.5, representing the wing is in the downstroke, and it is in the range of 0.5 to 1 for the upstroke.

CHAPTER 3. SIMULATION OF FLAPPING WINGS

In this chapter, a dynamic simulation is set up. Solutions of non-dimensional ODEs are solved by ode45 in MATLAB. To calculate lift-to-weight ratios and power loadings, we take data for the fruit fly from Weis-Fogh (1973), which were derived from studies of tethered flight (Vogel, 1966). Insect mass was 2 mg and the flapping frequency was 240 Hz. Finally a large parametric space is explored to predict how the wing trajectory change as stiffness coefficients change. The results also identify the wing trajectory pattern that may be considered better aerodynamic performance.

3.1 Numerical Simulation of Nonlinear Differential Equations

We use MATLAB's nonstiff ode45 solver to solve ODEs numerically. Ode 45 solve is based on an explicit Runge-Kutta formula (Dormand and Prince, 1980). Other solvers, such as nonstiff ode23, nonstiff ode113 and stiff ode15s, are also implemented in the simulation, and they return numerical results within relative tolerances of 10^{-5}. The state vector in ode 45 is

$$\boldsymbol{x}_{ode} = \begin{bmatrix} \phi & \theta & \psi & \omega_x & \omega_y & \omega_z \end{bmatrix}^T. \tag{3.2}$$

The initial condition of the state vector $\boldsymbol{x}_{ode,\,initial}$ is $\begin{bmatrix} 0 & 0 & 0 & 0 & 0 & 0 \end{bmatrix}^T$. The wing was positioned vertically at mid-stroke at the initial condition. No input torque ramp-up

was simulated, instead, the wing was accelerated from complete still to a steady state trajectory by the input torque at full speed. In the simulation, the wing is driven to flap for 40 wingbeats. The first 30 wingbeats is for getting rid of the effect from the initial condition. The solution for wing's Euler angles and angular velocities is obtained from the simulation results in the last 10 wingbeats. Then, we use the solutions and data for the fruit fly to calculate lift-to-weight ratios, power loadings, and aerodynamic force coefficients. An illustration of the simulation process is shown in Figure 3.2.

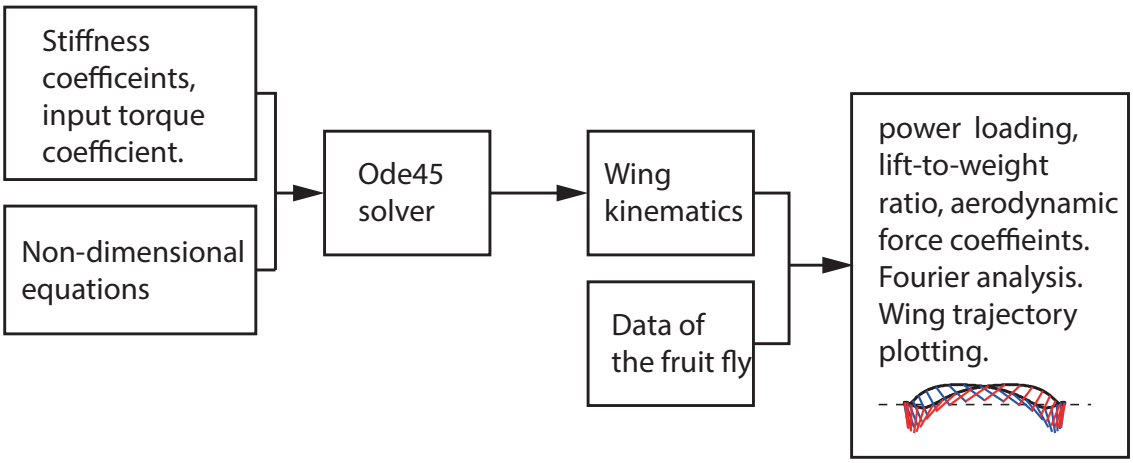

Figure 3.1. An illustration of the simulation process.

3.2 Parameter Space Search

In this section, we systematically vary rotation stiffness coefficient $\hat{k}_{\psi}$ and deviation stiffness coefficient $\hat{k}_{\theta}$. Stroke stiffness coefficient and input torque coefficient are constant values in parameter space search. Stiffness value of the stoke angle is designed

to achieve its approximate resonant motion. We assume that the wing is only one degree-of-freedom with stroke angle. Its approximate resonant frequency is given by:

$$2\pi f = \sqrt{\frac{k_\phi}{I_{zz}}}\,. \tag{3.3}$$

Substituting Equation 3.3 into Equation 2.80, stroke stiffness coefficient $\hat{k}_\phi$ becomes

$$\hat{k}_\phi = \frac{(2\pi)^2 I_{zz}}{I_{xx}}\,. \tag{3.4}$$

From Table 2.1, $\hat{k}_\phi$ = 33.92. All values of $\hat{M}_{max}$ in the range 17-27 could provide energy for system generating enough lift to fly. Rotation stiffness coefficient $\hat{k}_\psi$ ranges from 2 to 20, incremented by 2. Deviation stiffness coefficient $\hat{k}_\theta$ ranges from 30 to 2010, incremented by 20. Total number of simulated cases in the parameter space is 1000. Minimum values are selected when the systems couldn't generate a stable oscillatory flapping motion. The maximum value of $\hat{k}_\psi$ is selected when the rotation amplitude is less than 10 degrees under the driving of the input torque with a coefficient $\hat{M}_{max}$ = 21. The maximum value of $\hat{k}_\theta$ is selected when the rotation amplitude is less than 4 degrees.

After we get the simulation results, contour plots are generated using a cubic interpolation fitting method. Note that ranges in contour plots are smaller than ranges in simulation. Figure 3.2 shows the contour of lift-to-weight ratio and mean power loading as functions of deviation stiffness coefficient and rotation stiffness coefficient. We can see that the area of high lift and high power loading coincide for the parameters spanned

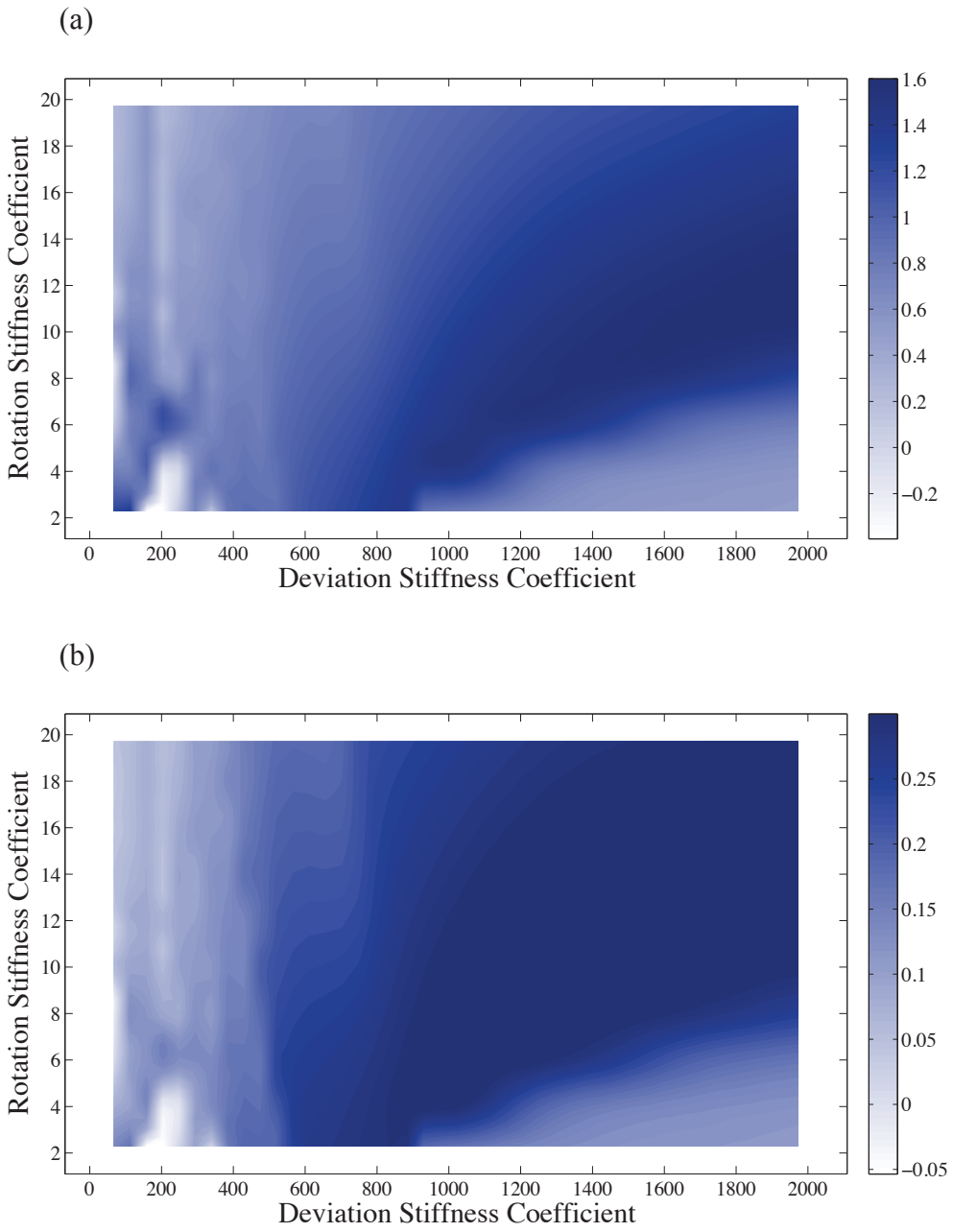

Figure 3.2. Contours of lift-to-weight ratio (a) and mean power loading (b) as functions of deviation stiffness coefficient and rotation stiffness coefficient. Dark shades indicate large values.

here. Contours of lift-to-weight ratio and mean power loading can be divided into four regions, as shown in Figure 3.3. One (region 1) is where the deviation stiffness coefficient $\hat{k}_\theta$ is less than 200 and the rotation stiffness coefficient $\hat{k}_\psi$ is less than 4. Lift-to-weight ratios in this region are larger than 1.0, and mean power loadings are about 0.15. However, the wing shows an erratic wing trajectory. The other one (region 2) is where $\hat{k}_\theta$ is between 200 and 600. Almost no lifts are generated in this region, and mean power loadings are almost zero. The biggest region (region 3) is where $\hat{k}_\theta$ is between 600 and 2010 and $\hat{k}_\psi$ is larger than 6. Mean power loadings are about 0.25 s/m and lift-to-weight ratios are about 1.4. The last one (region 4) is where $\hat{k}_\theta$ is large 1000 and 2010 and $\hat{k}_\psi$ is less than 6. This region has low lift-to-weight ratios and low mean power loadings.

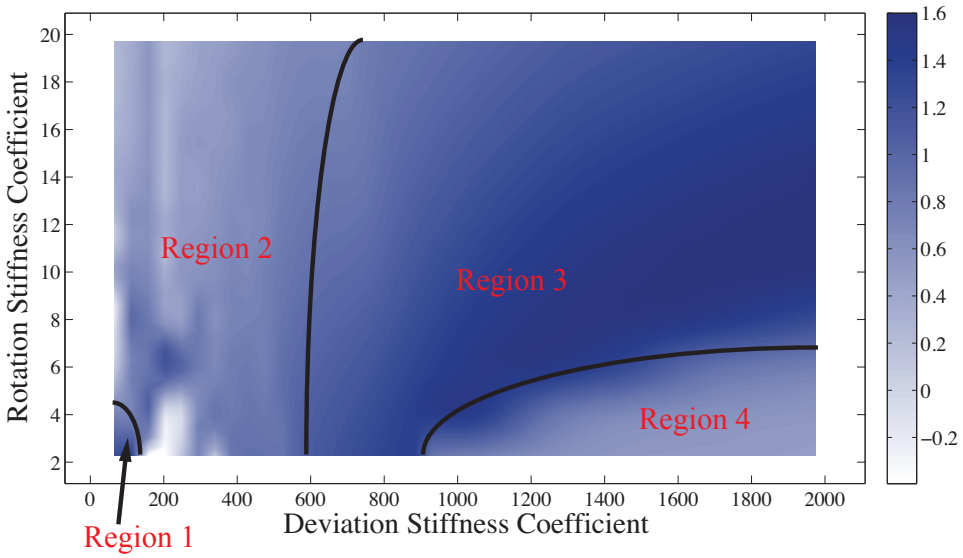

Figure 3.3. Four regions in contour of lift-to-weight ratio as functions of deviation stiffness coefficient and rotation stiffness coefficient. Dark shades indicate large values.

Table 3.1. Table of stiffness coefficients, lift-to-weight ratio and mean power loading in selected cases.

Symbol	R1	R2	R3	R4
$\hat{k}_{\phi}$	33.92	33.92	33.92	33.92
$\hat{M}_{max}$	21	21	21	21
$\hat{k}_{\theta}$	70	210	1410	1800
$\hat{k}_{\psi}$	2	14	8	4
$\overline{PL}$ (s/m)	0.1573	0.0658	0.3141	0.1350
L	1.35	0.12	1.56	0.59

Four cases (R1, R2, R3 and R4) are selected from each region, of which stiffness coefficients are list in Table 3.1. Wing trajectories of four cases are shown in Figure 3.4. Wing kinematics and aerodynamic force coefficients are plotted in Figure 3.5. We can see that only the wing in case R3 track an acceptable flapping trajectory, and trajectories in other three cases exhibits erratic. Case R1 has a large lift-to-weight ratio (L = 1.35), but a relative small power loading. The rotation angle exceeds 120 degrees and the deviation angle is between 17.3 and 49 degrees, due to the low rotation stiffness coefficient and the low deviation stiffness coefficient. Aerodynamics lift is positive at the beginning of the upstroke and the downstroke, and it is negative near the end of the upstroke and the downstroke. However, this pattern hasn't been reported by biology

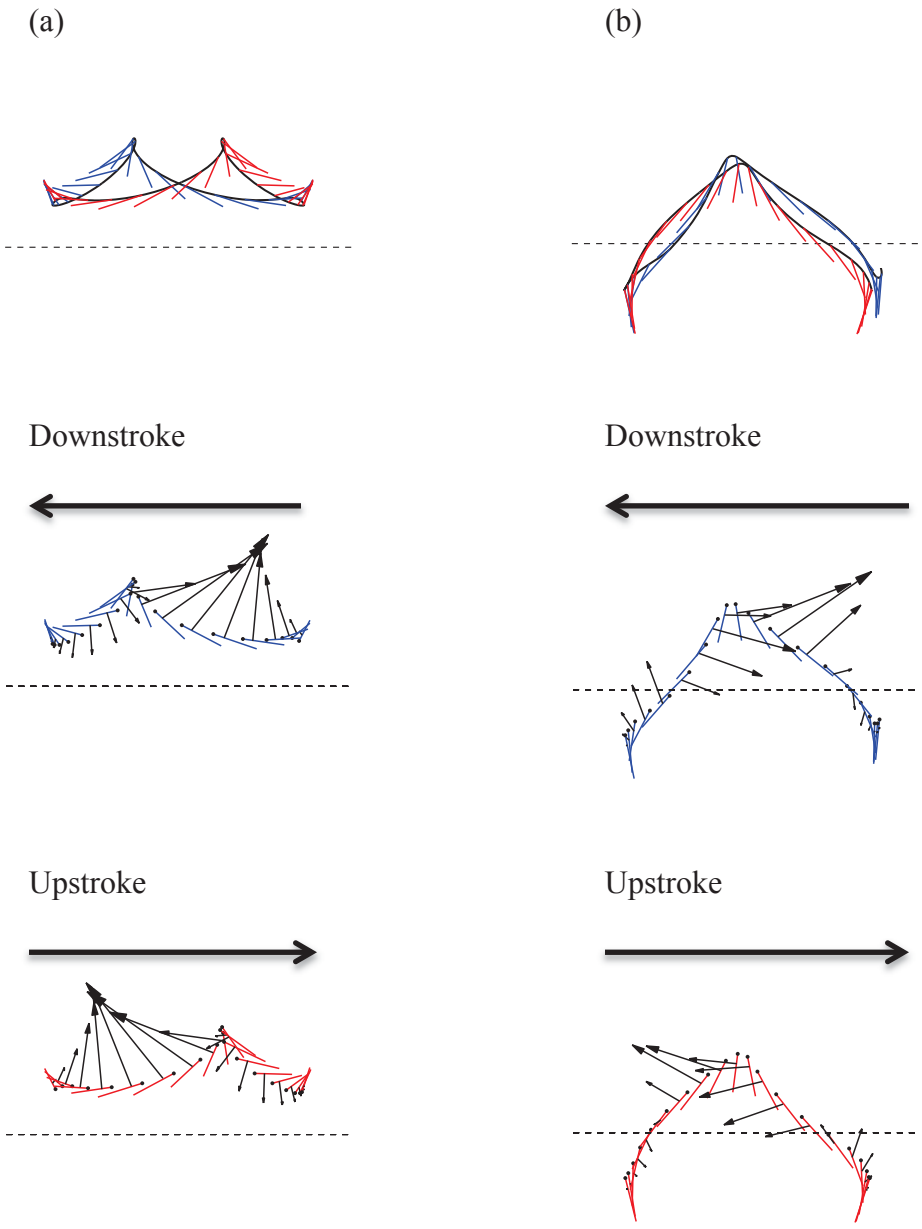

Figure 3.4. Wing trajectories of four cases. Wing cross section snapshots are portrayed and spaced 0.025/1 apart over the 40th stroke cycle. These lines represent the wing chord, and the dots represent the leading edges. The blue lines indicate the downstroke, and the red ones indicate the upstoke.

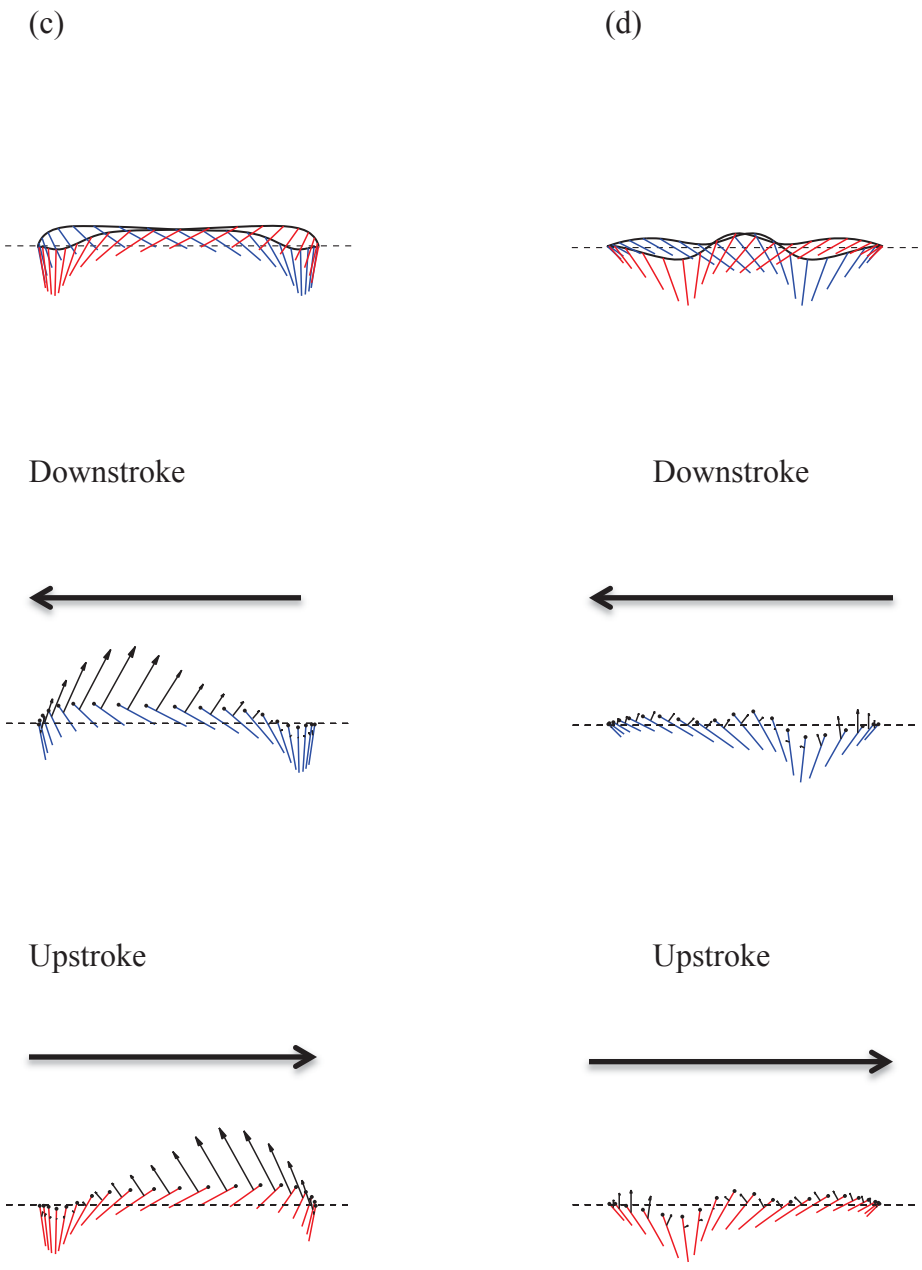

Figure 3.4: continued.

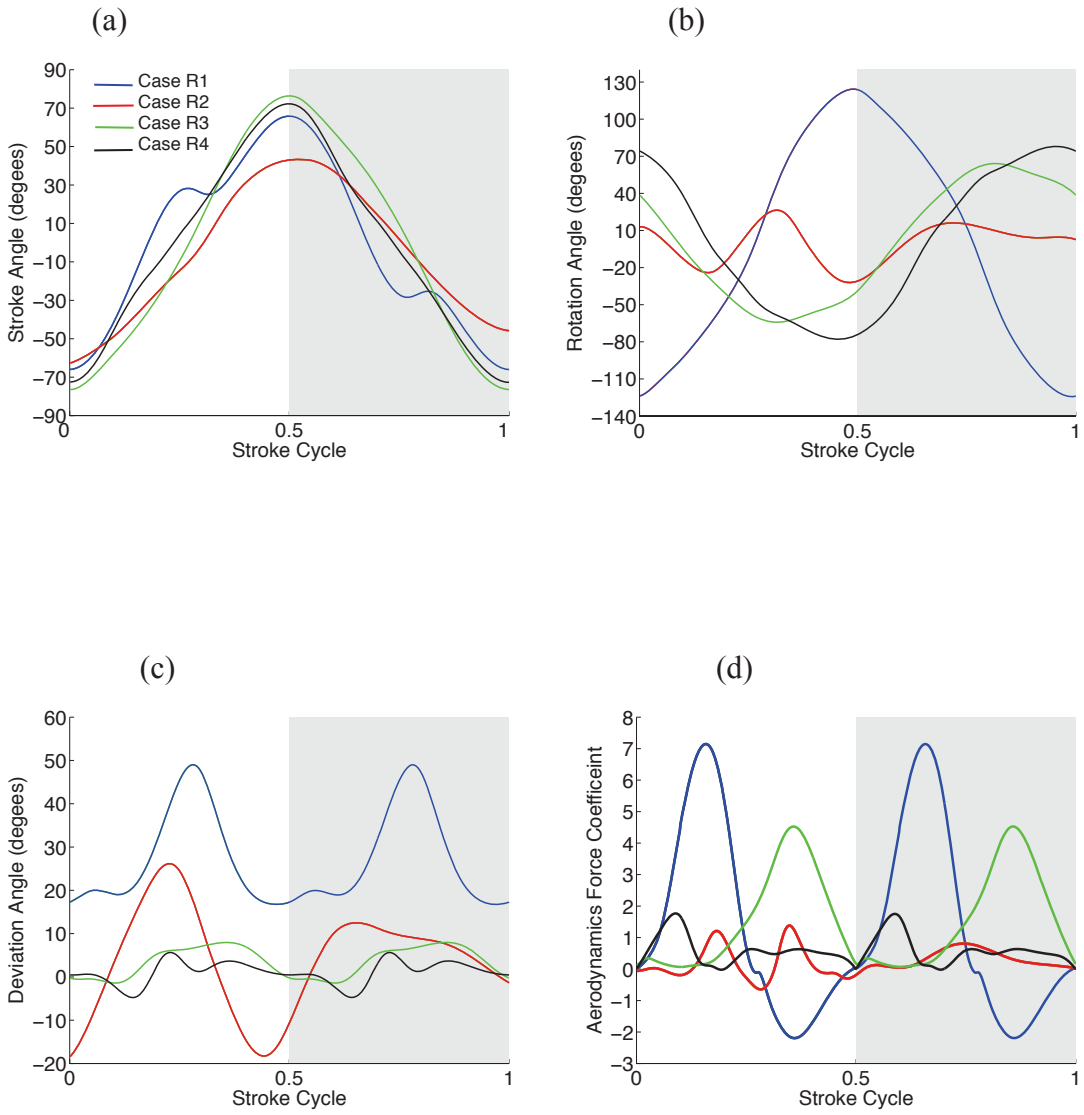

Figure 3.5. Wing kinematics and aerodynamic force coefficient versus stroke cycle during 40th stroke cycle. Case R1 is plotted in blue lines. Case R2 is plotted in red lines. Case R3 is plotted in green lines. Case R4 is plotted in black lines. The white region indicates the downstroke, and the grey region indicates the upstroke. (a) shows stroke angle v.s. stroke cycle, (b) shows rotational angle v.s. stroke cycle and (c) shows deviation angle v.s. stroke cycle. (d) shows aerodynamic force coefficient v.s. stroke cycle.

studies. The wing trajectory in Case R2 is non-symmetrical. Figure 3.6 shows wing trajectories of case R2 and case R3 from 31th to 40th stroke cycles. Trajectories don't show any stable property. Aerodynamics force is always in the non-effective direction, rather than vertically up. The stoke amplitude of case R3 is 72.2 degrees and the rotation amplitude is 64.0 degrees. The maximum value of the deviation is 7.9 degrees. As the wing maintains an effective AOA, aerodynamic lift is generated during the upstroke and the downstroke. When the wing is accelerating, no much force is generated. A peak appears near the end of the stroke, and the wing is decelerating. In Figure 3.5(d), the aerodynamic lift of case R3 is still above zero even at the beginning and near the end of the upstroke and the downstroke. Case R4 has a small rotation stiffness coefficient and a large deviation stiffness coefficient. The lift-to-weight ratio is only 0.59, as the wing couldn't have an effect AOA during flapping. It hasn't been reported by biology studies, neither.

Since the amplitude of the stroke angle has a direct relationship with the generation of aerodynamic lift, it is of interest to see how the amplitude of stroke angle changes at the stable region. Figure 3.7 shows the contour of amplitude of the stroke angle as functions of deviation stiffness coefficient and rotation stiffness coefficient, where $\hat{k}_\theta$ is between 610 and 2000. Other contours of amplitude of the stroke angle, the rotation angle and the deviation angle where $\hat{k}_\theta$ is between 30 and 2010 and $\hat{k}_\psi$ is between 2 and 20 are in Appendix B. We can see that the area of high lift and large amplitude coincide for the parameters spanned. The amplitude is larger than 75 degrees, when $\hat{k}_\theta$ is larger 1600 and $\hat{k}_\psi$ is between 6 and 10.

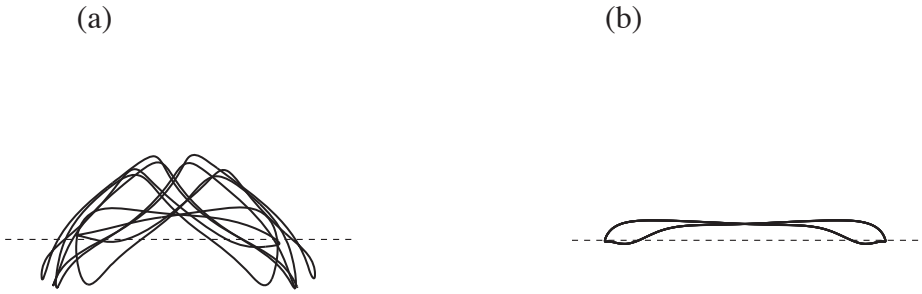

Figure 3.6. Wing trajectories portrayed from 31th to 40th stroke cycles. The dots represent the leading edges. (a) shows case R2. (b) shows Case R3.

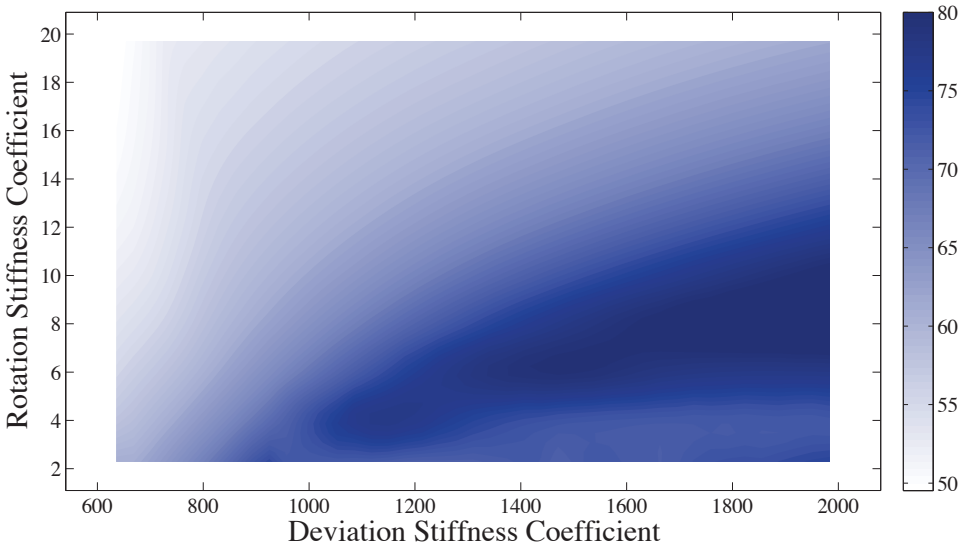

Figure 3.7. Contours of amplitude of the stroke angle as functions of deviation stiffness coefficient and rotation stiffness coefficient. Dark shades indicate large values.

It is summarized that (1) a low deviation stiffness coefficient and a low rotation stiffness coefficient show erratic wing trajectories; (2) The case with a high deviation stiffness coefficient and a mediate rotation stiffness coefficient can produce sufficient lift

to support the weigh while achieving higher power loading. Its wing trajectory is close to the wing trajectory in actual insect.

CHAPTER 4. OPTIMIZATION OF FLAPPING WINGS

Given the dynamic model of the oscillation system described in the previous sections, we optimize stiffness coefficients of torsional springs. We first introduce the optimization algorithm, a hybrid algorithm of a genetic algorithm and a Nelder-Mead simplex algorithm. Then two different categories are investigated. Category A includes two optimization parameters, which are stroke stiffness coefficient $\hat{k}_\phi$, and rotation stiffness coefficient $\hat{k}_\psi$. In this situation, deviation stiffness coefficient $\hat{k}_\theta$ is set 50000 to limit the motion in the deviation angle. Category B considers the effect of the deviation angle, where optimization parameters are $\hat{k}_\phi$, $\hat{k}_\psi$ and $\hat{k}_\theta$. We denote $\boldsymbol{x}$ as the state vector in optimization. n is the number of variables in $\boldsymbol{x}$. For category A, $\boldsymbol{x} = \begin{bmatrix} \hat{k}_\phi & \hat{k}_\psi & \hat{k}_\theta \end{bmatrix}^T$ and n = 3. For category B, $\boldsymbol{x} = \begin{bmatrix} \hat{k}_\phi & \hat{k}_\psi \end{bmatrix}^T$ and n = 2. Input torque coefficient $\hat{M}_{max}$ is varied from 17 to 27. Compared these two categories, we can get an insight of how different wing trajectories are generated and figure out what kind of wing trajectories patterns achieves a higher hovering efficiency.

4.1 Optimization Technique

Classical algorithms, such as gradient methods, Newton's method, conjugate gradient methods and quasi-Newton methods are not suitable in this situation, as it is difficult to calculate the derivatives. The genetic algorithm and the Nelder-Mead simplex algorithm, which use only objective function values and do not require derivatives, are applicable to this optimization problem. The optimization procedure is a hybrid of these two algorithms. The genetic algorithm is started with a population of parameter sets that are then evolved to be grouped in a globally minimal basin. The genetic algorithm can reach the region near an optimum point relatively quickly, but it may be take many function evaluations to achieve convergence. To avoid this situation, the genetic algorithm is run for a small number of generations to get near the optimum point. The solution from the genetic algorithm is not global optimum, and it is then used as an initial point for the Nelder-Mead simplex algorithm that is faster and more efficient for the local search of the basin. We validate all of the results by multiple runs of the algorithm.

As presented above, biology studies have found that the stiffness of the system could be changed somewhat by the action of small accessory muscles in the thorax (Nachtigall and Wilson, 1967; Josephson, 1981; Tu and Dickinson, 1996). Stiffness coefficients of each Euler angle, which are $\hat{k}_\phi$, $\hat{k}_\psi$ and $\hat{k}_\theta$, are chosen as optimization parameters. The ranges of $\hat{k}_\phi$, $\hat{k}_\psi$ and $\hat{k}_\theta$ are shown in Table 4.1. They are selected based results in Section 3.2. The problem also is constrained by the physical limitations on the parameters listed in Table 4.1. A wide range is available to the insect under these constraints, and a selection of possible wing kinematics is shown in Figure 4.1.

Table 4.1. Table of optimized parameters and their ranges.

Symbol	Description	Min	Max
$\hat{k}_{\phi}$	stroke stiffness coefficient	20	200
$\hat{k}_{\theta}$	deviation stiffness coefficient	30	7000
$\hat{k}_{\psi}$	rotation stiffness coefficient	2	50
$\lvert\phi\rvert_{max}$	stroke amplitude	0	$\pi/2$
$\lvert\theta\rvert_{max}$	deviation amplitude	0	$\pi/2$
$\lvert\psi\rvert_{max}$	rotation amplitude	0	$\pi/2$

The objective function is defined to find the minimum of the power usage while the wing still produce enough lift to maintain hovering flight. It should be note that the objective function in the genetic algorithm is different from the one in the Nelder-Mead simplex algorithm. The genetic algorithm could effectively handle the discontinuous function, but it would become very slowly convergent when facing the function with nonlinear inequality constraints. The Nelder-Mead simplex algorithm couldn't handle this unconstrained and discontinuous optimization, especially if the solution occurs near the discontinuity. Therefore different objective functions are designed for the genetic algorithm and the Nelder-Mead simplex algorithm to increase the efficiency of the hybrid algorithm.

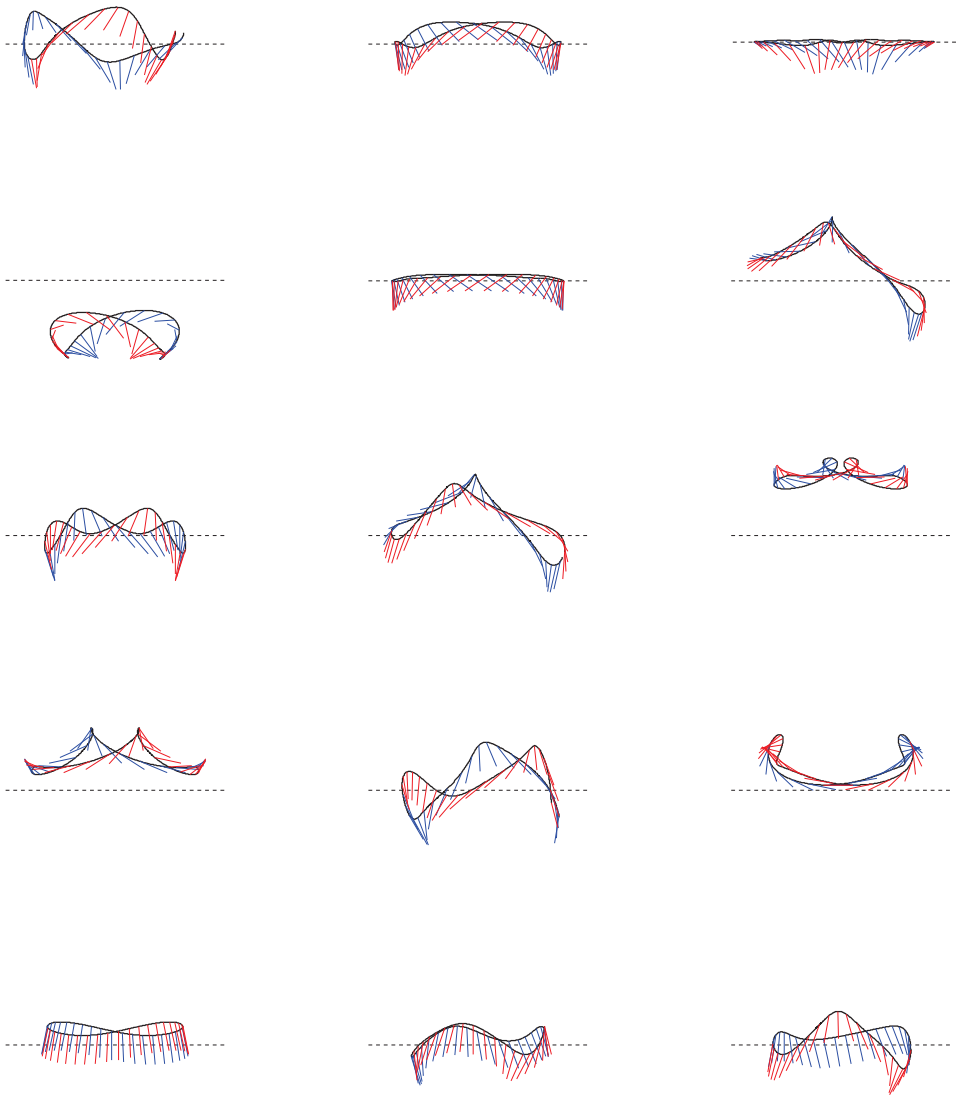

Figure 4.1. A selection of possible wing kinematics. Wing cross section snapshots are portrayed and spaced 0.025/1 apart over the one stroke cycle. These lines represent the wing chord, and the dots represent the leading edges. The blue lines indicate the downstroke, and the red ones indicate the upstoke.

Considering the constraints, the optimization in the genetic algorithm is converted into a more tractable problem by defining the objective function, f_{ga} by:

$$f_{ga} = -\overline{PL} + \chi\Theta(1-L) + \sum_{\zeta\in\boldsymbol{\gamma}} \chi\Theta\left(\zeta - Max_{\zeta}\right) + \sum_{\zeta\in\boldsymbol{\gamma}} \chi\Theta\left(Min_{\zeta} - \zeta\right) \tag{3.5}$$

where $\Theta(\ )$ is the Heaviside step function, that is a discontinuous function whose value is one for positive argument and zero for negative argument. ζ is in parameters set $\boldsymbol{\gamma}$. From Table 4.1, we have $\boldsymbol{\gamma} = \left\{|\phi|_{max}, |\psi|_{max}, |\theta|_{max}\right\}$. Note that $\boldsymbol{\gamma}$ is not a set of optimization parameters, but results from ode45 solvers. Max_{ζ} is denoted as the maximum value of ζ, and Min_{ζ} is denoted as the minimum value of ζ. χ is positive, real parameters which specify the strength of the penalty for violating the lift and physical constraints. We set χ = 2000. The results from the genetic algorithm suggest that the optimal motions are that they produce just above enough lift to hover L = 1, which is near the edge of the discontinuity in the Heaviside step function. Therefore we couldn't use the same object function in the next optimization phase. For the Nelder-Mead simplex algorithm, the optimization problem should be continuous in the space. The objective function is defined as:

$$f_{NM} = -\overline{PL} \tag{3.6}$$

with the lower bound constraint

$$Min_{\zeta} \le \zeta \tag{3.7}$$

and the nonlinear inequality constraint:

$$L \ge 1. \tag{3.8}$$

The reason to choose the lower bound constraints instead of the dual bound constraints will be discussed in Section 4.3. The detail of how to setup the genetic algorithm and the Nelder-Mead simplex algorithm are present in the following section.

4.2 Genetic Algorithms Setup

A genetic algorithm (GA) is a method for solving both constrained and unconstrained optimization problems based on a natural selection process that mimics biological evolution. The beginning of genetic algorithms is credited to John Holland, who developed the basic ideas in the late 1960s and early 1970s. Since its conception, genetic algorithms have been used widely as a tool in computer programming and artificial intelligence (Holland, 1992; Kora, 1992; Mitchell, 1996), optimization (Davis, 1987; Jang, *et al.*, 1997; Then and Chong, 1994), neural network training (Kozek, 1993), and many other areas. The genetic algorithm differs from classical algorithms, such as Newton's method and gradient method, in several respects. First, it doesn't use derivatives of the objective function. Second, it uses operations that are random at each iteration. Third, it searches from a set of points rather than a single point.

Suppose that we wish to solve an optimization problem that is to find the minimum value of $f_{ga}(\boldsymbol{x})$, where $\boldsymbol{x} \in \Omega$. In category A, $\boldsymbol{x} = \begin{bmatrix} \hat{k}_\phi & \hat{k}_\psi \end{bmatrix}^T$, and in category B, $\boldsymbol{x} = \begin{bmatrix} \hat{k}_\phi & \hat{k}_\psi & \hat{k}_\theta \end{bmatrix}^T$. The process of genetic algorithms is shown as follows. We start with an initial set of points in Ω, denoted $P(0)$, called the initial population. We then evaluate the objective function at points in $P(0)$, and create a new set of points $P(1)$. At

each step, the genetic algorithm selects individuals from the current population $P(k)$ based on the notion of "survival of the fittest", and uses operations, called crossover and mutation, to produce the next generation $P(k+1)$. The purpose of the crossover and mutation operation is to create a new population with an average objective function value that is higher than that of the previous population. Over successive generations, the population evolves toward an optimal solution. In the following section, we discuss the details of the algorithm.

The first step is the identification of appropriate representation scheme including the choice of chromosome length, alphabet and encoding. The genetic algorithm does not work directly with points in the set Ω, but rather with an encoding of points in Ω. We need to map Ω onto a set consisting of string of symbols, all of equal length. These strings are called chromosomes. Each chromosome consists of elements from a chosen set of symbols, called the alphabet. The chromosomes are chosen as binary strings, and the alphabet is the set $\{0,1\}$. We denote by L_{ga} the length of chromosome (i.e., the number of symbols in the strings). The default data type in MATLAB is double-precision binary floating-point that is 64 bits. We set the relative tolerances of all parameters 10^{-7} in the genetic algorithm and use a simple binary representation scheme with length $L_{ga} = 32n$. 32 bits of each chromosome encode one optimization variable. The interval $[20, 200]$ for $\hat{k}_{\phi}$, $[2, 50]$ for $\hat{k}_{\psi}$ and $[30, 7000]$ for $\hat{k}_{\theta}$ are mapped onto the interval $[0, 2^{32}-1]$ via a simple translation and scaling, respectively. The integers in the interval

$\left[0, 2^{32}-1\right]$ are then expressed as binary 32-bit strings. This defines the encoding of each component $\hat{k}_\phi$, $\hat{k}_\theta$ and $\hat{k}_\psi$. The chromosome is obtained by juxtaposing the n 32-bit strings.

Once a suitable representation scheme has been chosen, the next step is to define the population size. The population size, which we denote by N, specifies how many individuals there are in each generation. With a large population size, the genetic algorithm searches the solution space more thoroughly, thereby reducing the chance that the algorithm will return a local minimum that is not a global minimum. However, a large population size also causes the algorithm to run more slowly. We choose $N_{ga} = 10n$. Then the first population $P(0)$ of chromosomes is initialized through a random selection with a uniform distribution in the range. We then apply the operations of crossover and mutation on the population. During each iteration *k* of the process, we evaluate the fitness $g\left(\boldsymbol{x}^{(k)}\right)$ of each member $\boldsymbol{x}^{(k)}$ of the population $P(k)$. Note that the fitness function $g\left(\boldsymbol{x}^{(k)}\right)$, a fitness measure on the set of chromosomes, is different from the objective function $f_{ga}\left(\boldsymbol{x}^{(k)}\right)$. After the fitness of the entire population has been evaluated, we form a new population $P(k+1)$ in two stages. The first stage is called selection and the second one is called evolution.

In the first stage, we define the fitness function, and then apply an operation called selection. The fitness function is to converts the raw fitness scores that are returned by the objective function to values in a range that is suitable for the selection operation. The

selection function uses the scaled fitness values to select the parents of the next generations, and assigns a higher probability of selection to individuals with higher scaled values. The range of the scaled values affects the performance of the genetic algorithm. If the scaled values vary too widely, the individuals with the highest scaled values reproduce too rapidly, taking over the population pool too quickly, and preventing the genetic algorithm from searching other areas of the solution space. On the other hand, if the scaled values vary only a little, all individuals have approximately the same chance of reproduction and the search will progress very slowly.

The fitness scaling function, called rank method, is applied here, which scales the raw scores based on the rank of each member instead of its score. We get

$$g\left(\boldsymbol{x}^{(k)}\right)=\frac{\frac{1}{\sqrt{r}}}{1+\frac{1}{\sqrt{2}}+\cdots+\frac{1}{\sqrt{n}}}N, \tag{3.9}$$

where r is the rank of the member in the sorted scores. The scaled score of the most fit member is proportional to 1, the scaled score of the next most fit is proportional to $1/\sqrt{2}$, and so on. A member with rank r has scaled score proportional to $1/\sqrt{r}$. The sum of the scaled values over the entire population equals the number of the population size. Rank fitness scaling removes the effect of the spread of the raw scores from the objective function.

The selection scheme called roulette-wheel scheme is applied in our optimization problem. A set $M\left(k\right)$, called the mating pool with N elements, is formed from $P\left(k\right)$

using a random procedure as follows: Each point $\boldsymbol{m}^{(k)}$ in $M(k)$ is equal to $\boldsymbol{x}^{(k)}$ in $P(k)$ with probability

$$P_{mating}\left(\boldsymbol{m}^{(k)}\right)=\frac{\frac{1}{\sqrt{r}}}{1+\frac{1}{\sqrt{2}}+\cdots+\frac{1}{\sqrt{n}}}. \tag{3.10}$$

This means that chromosomes are selected into the mating pool with probabilities proportional to their fitness values.

In the second stage we apply the crossover and mutation operations. The crossover operation takes a pair of chromosomes, called the parents, and gives a pair of offspring chromosomes. The operation involves exchanging substrings of the two parent chromosomes. Pairs of parents for crossover are chosen form the mating pool randomly, such that the probability that a chromosome is chosen for crossover is p_c. Here we set $p_c = 2/N_{ga}$. Additionally, we assume that whether or not a given chromosome is chosen is independent of whether or not any other chromosome is chosen for crossover. A chromosome can be selected more than once as a parent, in which case it contributes its string to more than one child.

Once the pairs of the parents for crossover have been determined, the crossover operation is applied. There are many types of possible crossover operations. The one we used here is the scattered crossover (Goldberg, 1989). A random binary vector is created according to a uniform distribution. The first substring is selected where the vector is a 1 from the first parent, and the second substring is selected where the vector is a 0 from the second parent. The first child is formed through combining these two substrings. Two

left substrings form the second child. For example, $p1$ and $p2$ are parents and $c1$ and $c2$ are children. Parents are

$$p1 = \begin{bmatrix} A & B & C & D \end{bmatrix}, \tag{3.11}$$

$$p2 = \begin{bmatrix} a & b & c & d \end{bmatrix}. \tag{3.12}$$

If the random binary vector is $\begin{bmatrix} 1 & 0 & 1 & 1 \end{bmatrix}$, the first child is given by

$$c1 = \begin{bmatrix} A & b & C & D \end{bmatrix}. \tag{3.13}$$

The second child is

$$c2 = \begin{bmatrix} a & B & c & d \end{bmatrix}. \tag{3.14}$$

After the crossover operation, we replace the parents in the mating pool by their offspring. In this way, the mating pool has been modified but maintains the same number of elements.

Next, we apply the mutation operation, which takes each chromosome from the mating pool and randomly changes each symbol of the chromosome with a given probability p_m. In the case of the binary alphabet, this change corresponds to complementing the corresponding bits; that is, we replace each bit with probability p_m from 0 to 1, or vice versa. Typically, the value of p_m is very small. We choose $p_m = 0.01$. We can see that only a few chromosomes will undergo a change due to mutation, and of those that are affected, only a few of the symbols are modified. The mutation operation plays only a minor role in the genetic algorithm relative to the crossover operation.

After the selection and evolution stages, the final $M(k)$ is the new population $P(k+1)$. We then repeat the procedure of selection, crossover and mutation, iteratively until the stopping criterion is met. Two stopping criterions are implemented, and the genetic algorithm would stop when either one is satisfied. On stopping criterion is to stop when the fitness for the best-so-far chromosome does not change significantly from iteration to iteration. The tolerance is set to 10^{-8}. The other criterion is to stop when the algorithm reaches the maximum number of iterations, which is 50 here.

Overall, the genetic algorithm iteratively performs the operations of crossover and mutation on each population to produce a new population until a chosen stopping criterion is met. A flowchart illustrating the genetic algorithm is shown in Figure 4.2. It is summarize as follows:

1. Set $k := 0$. Generate an initial population $P(k)$.
2. Evaluate $P(k)$.
3. Scale the evaluation.
4. If the stopping criterion is satisfied, then stop.
5. Select $M(k)$ from $P(k)$.
6. Evolve $M(k)$ to form $P(k+1)$.
7. Set $k := k+1$, go to step 2.

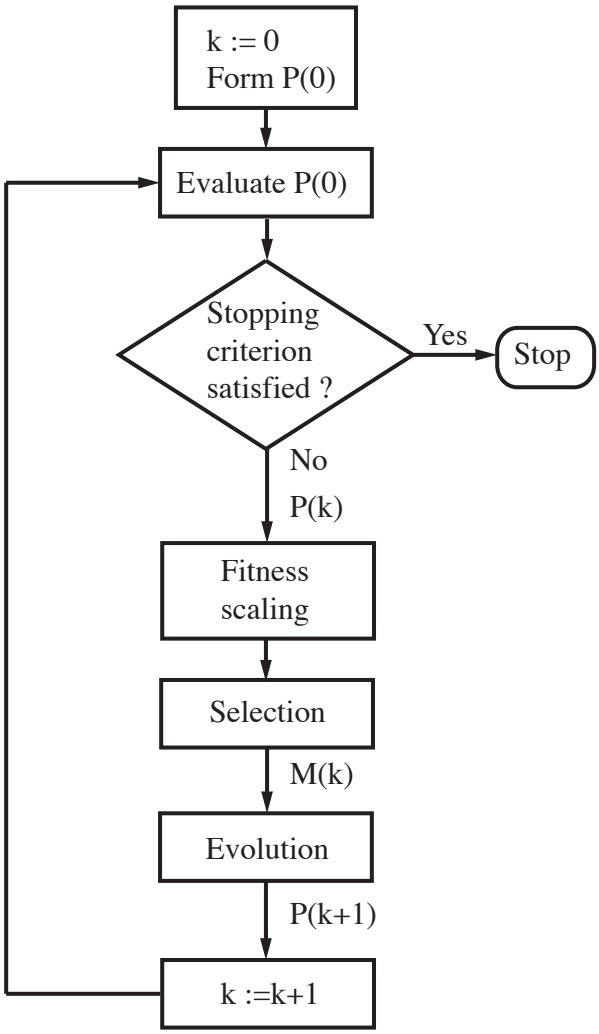

Figure 4.2. Flowchart for the genetic algorithm.

4.3 Nelder-Mead Simplex Algorithm Setup

The method originally proposed by Spendley, Hext, and Himsworth (1962) was improved by Nelder and Mead (1965) and it is now commonly referred to as the Nelder-

Mead simplex algorithm. A contemporary view of the algorithm is provided by Lagarias *et al.* (1998).

The Nelder-Mead simplex algorithm is a derivative-free method that uses the concept of a simplex. In category A, $\boldsymbol{x}_i = \begin{bmatrix} \hat{k}_\phi & \hat{k}_\psi \end{bmatrix}^T$. In category B, $\boldsymbol{x}_i = \begin{bmatrix} \hat{k}_\phi & \hat{k}_\psi & \hat{k}_\theta \end{bmatrix}^T$. A simplex is a geometric object determined by an assembly of n+1 points, $\boldsymbol{x}_0$, $\boldsymbol{x}_1$, $\cdots$, $\boldsymbol{x}_n$, in the n-dimensional space such that

$$det\begin{bmatrix} \boldsymbol{x}_0 & \boldsymbol{x}_1 & \cdots & \boldsymbol{x}_n \\ 1 & 1 & \cdots & 1 \end{bmatrix} \neq 0. \tag{3.15}$$

This condition ensures that two points in R do not coincide, three points in R^2 are not collinear, four points in R^3 are not coplanar, and so on. Thus, the simplex is a line segment in R, in R^2 it is a triangle, while a simplex in R^3 is a tetrahedron; in each case it encloses a finite n-dimensional volume.

We now present how to modify the simplex stage by stage. First, a transformation of the variable is built to implement lower and upper bound constraints. After getting the unconstraint variables in the new space, we setup the optimization engine, which is the simplex modification. Then general linear inequality constraints and nonlinear inequality constraints are implemented as penalty functions, to make sure that the objective function would never be evaluated outside of the supplied constraints.

We begin by implementing lower and upper bound constraints by the careful use of transformations of the variables. The idea is to insert a wrapper function about the original objective function. There are several classes of bound constraints we might consider. They are lower bound constraints

$$\boldsymbol{x}_{min} \leq \boldsymbol{x}_i , \tag{3.16}$$

upper bound constraints

$$\boldsymbol{x}_i \leq \boldsymbol{x}_{max} , \tag{3.17}$$

and dual constraints

$$\boldsymbol{x}_{min} \leq \boldsymbol{x}_i \leq \boldsymbol{x}_{max} , \tag{3.18}$$

where $\boldsymbol{x}_{min}$ is the vector of minimum values $\boldsymbol{x}_i$ can achieve, and $\boldsymbol{x}_{max}$ is the vector of maximum values. The bounded variables are transformed such that the simplex modification handles a fully unconstrained problem. Difference transformation functions can be designed here. In the case of a variable bounded on the lower end by $\boldsymbol{x}_{min}$, we choose to use the transformation

$$\boldsymbol{x}_i = \boldsymbol{x}_{min} + \tilde{\boldsymbol{x}}_i^2 , \tag{3.19}$$

where variable $\tilde{\boldsymbol{x}}_i$ is fully unconstrained and is always non-negative. Likewise, a pure upper bound constraint is implemented as

$$\boldsymbol{x}_i = \boldsymbol{x}_{max} - \tilde{\boldsymbol{x}}_i^2 . \tag{3.20}$$

Clearly, $\boldsymbol{x}_i$ can never rise about $\boldsymbol{x}_{max}$. The dual bounded variable is handled by a trigonometric transformation:

$$\boldsymbol{x}_i = \boldsymbol{x}_{min} + \frac{1}{2}\left(sin\left(\tilde{\boldsymbol{x}}_i\right)+1\right)\left(\boldsymbol{x}_{max} - \boldsymbol{x}_{min}\right) . \tag{3.21}$$

In this case, we enforce the requirement that $\boldsymbol{x}_{min} \leq \boldsymbol{x}_i \leq \boldsymbol{x}_{max}$. An artifact of the transformations used here is the creation of multiple solutions to a problem that at one time may well have had a unique solution. While the presence of multiple local solutions

is often a problem for an optimizer, each of these introduced solutions is fully equivalent. It maybe not matter which one is found in the last. To alleviate this problem, we only consider the lower bound constraints in the Nelder-Mead simplex algorithm and implement Equation 4.11.

We next select the initial set of n+1 points that are to form the initial simplex. A way to set up a simplex is to start with an initial point and generate the remaining points of the initial simplex as follows (Jang *et al.* 1997):

$$\tilde{\boldsymbol{x}}_i = \tilde{\boldsymbol{x}}_0 + \lambda_i \boldsymbol{e}_i , \tag{3.22}$$

where $i = 0, 1, \cdots, n$ and $\boldsymbol{e}_i$ are unit vectors the natural basis of R^n. The positive constant coefficients λ_i are selected in such a way that their magnitudes reflect the length scale of the optimization problem. We choose $\lambda_i = 0.05$.

Next, we evaluate f_{NM} at each point $\tilde{\boldsymbol{x}}_i$, and order the n+1 vertices from lowest function value to highest

$$f_{NM}(\boldsymbol{p}_0) \le f_{NM}(\boldsymbol{p}_1) \le \cdots \le f_{NM}(\boldsymbol{p}_n), \tag{3.23}$$

where $\boldsymbol{p}_0, \boldsymbol{p}_1, \cdots, \boldsymbol{p}_n$ is a order list for each simplex. In category A, $\boldsymbol{p}_i = \begin{bmatrix} \hat{k}_\phi & \hat{k}_\psi \end{bmatrix}^T$. In category B, $\boldsymbol{p}_i = \begin{bmatrix} \hat{k}_\phi & \hat{k}_\psi & \hat{k}_\theta \end{bmatrix}^T$. f_i denote the objective function value corresponding to the point $\boldsymbol{p}_i$. $\boldsymbol{p}_0$, $\boldsymbol{p}_{n-1}$, and $\boldsymbol{p}_n$ are the points of the simplex for which f_{NM} is largest, next largest, and smallest.

We denote $\boldsymbol{p}_g$ as the centroid of the best n points that is given by

$$\boldsymbol{p}_g = \sum_{i=0}^{n-1} \frac{\boldsymbol{p}_g}{n}. \tag{3.24}$$

We then reflect the worst vertex, $\boldsymbol{p}_l$, in $\boldsymbol{p}_g$ using a reflection coefficient to obtain the reflection point

$$\boldsymbol{p}_r = \boldsymbol{p}_g + \left(\boldsymbol{p}_g - \boldsymbol{p}_n\right). \tag{3.25}$$

We proceed to evaluate f_{NM} at $\boldsymbol{p}_r$ to obtain $f_{NM,r} = f_{NM}\left(\boldsymbol{p}_r\right)$.

If $f_{NM,0} \le f_{NM,r} < f_{NM,n-1}$, then the point $\boldsymbol{p}_r$ replace $\boldsymbol{p}_n$ to form a new simplex, and we terminate the iteration. We proceed to repeat the process. Thus, we compute the centroid of the best n vertices of the new simplex and again reflect the point with the worst function f value in the centroid obtained for the best n points of the new simplex. However, if $f_{NM,r} < f_{NM,0}$, so that the point $\boldsymbol{p}_r$ becomes the smallest function value among the points of the simplex, this direction is a good one and the algorithm should do expansion operation. In this case, we use an expansion coefficient to obtain

$$\boldsymbol{p}_e = \boldsymbol{p}_g + 2\left(\boldsymbol{p}_r - \boldsymbol{p}_g\right). \tag{3.26}$$

The operation yields a new point on the line $\boldsymbol{p}_n\boldsymbol{p}_g\boldsymbol{p}_r$ extended beyond $\boldsymbol{p}_r$. If $f_{NM,e} < f_{NM,r}$, the expansion is declared a success and $\boldsymbol{p}_n$ is replaced by $\boldsymbol{p}_e$ in the next simplex. On the other hand, if $f_{NM,e} \ge f_{NM,r}$, the expansion is declared a failure and $\boldsymbol{p}_n$ is replaced by $\boldsymbol{p}_r$.

Finally, if $f_{NM,r} \ge f_{NM,n-1}$, the reflexed point $\boldsymbol{p}_r$ would constitute the point with largest function value in the next simplex. Then in the next step it would be reflected in

$\boldsymbol{p}_g$, probably an unfruitful operation. In this case, a contraction operation is applied. If $f_{NM,n-1} \le f_{NM,r} < f_{NM,n}$, we obtain contract $\left(\boldsymbol{p}_r - \boldsymbol{p}_g\right)$ with a contraction coefficient to obtain

$$\boldsymbol{p}_c = \boldsymbol{p}_g + 0.5\left(\boldsymbol{p}_r - \boldsymbol{p}_g\right). \tag{3.27}$$

This operation is called the outside contraction. If $f_{NM,r} \ge f_{NM,n}$, then $\boldsymbol{p}_n$ replaces $\boldsymbol{p}_r$ in the contraction operation and we get

$$\boldsymbol{p}_c = \boldsymbol{p}_g + 0.5\left(\boldsymbol{p}_n - \boldsymbol{p}_g\right). \tag{3.28}$$

This operation is called the inside contraction. If, in either case, $f_{NM,c} \le f_{NM,n}$, the contraction is declared a success, and the $\boldsymbol{p}_n$ is replaced by $\boldsymbol{p}_c$ in the next simplex.

If $f_{NM,c} > f_{NM,n}$, the contraction is considered as a failure. In this situation, the shrink operation is applied. A new simplex is formed by retaining $\boldsymbol{p}_0$ only and halving the distance from $\boldsymbol{p}_0$ to every other point in the simplex. The shrink operation produces the *n* new vertices of the new simplex according to the formula

$$\boldsymbol{v}_i = \boldsymbol{p}_s + 0.5\left(\boldsymbol{p}_i - \boldsymbol{p}_s\right), \tag{3.29}$$

where $i = 0, 1, \cdots, n$. The vertices of the new simplex are $\boldsymbol{p}_0$, $\boldsymbol{v}_1$, $\cdots$, $\boldsymbol{v}_n$ which is used in the next iterative loop.

We also need to consider the nonlinear inequality constraints $L \ge 1$. If the operation of the simplex modification would have tried to evaluate the objective function outside the bounds, the infinity value is returned to f_{NM}, rather than the value from the objective

function. These constraints are implemented as penalty functions. In this way, the objective function will be always evaluated inside of the supplied constraints. The process above stop until the diameter of the simplex is less than the specified tolerance, which is 10^{-8}.

We summarize the Nelder-Mead simplex algorithm as follows.

1. Transform the variables into unconstraint conditions.
2. Form the initial simplex.
3. Order according to the values at the vertices.
4. If the stopping criterion is satisfied, then stop.
5. Calculate the center of gravity of all points except the best point.
6. Reflection.
7. If the reflected point is better than the second worst, but not better than the best, then obtain a new simplex by replacing the worst point with the reflected point, and go to step 3.
8. If the reflected point is the best point so far, go to step 7.
9. If the reflected point is not better than the second worst, go to 8.
10. Expansion.
11. If the expanded point is better than the reflected point, then obtain a new simplex by replacing the worst point with the expanded point, and go to step 3.
12. Else, then obtain a new simplex by replacing the worst point with the reflected point, and go to step 3.
13. Contraction.

14. If the reflected point is better than the worst, the contraction point is got by outside contraction. Else the contraction point is got by inside contraction. If the contraction is better than the worst, replace the worst point, and go to step 3. Else go to step 9.
15. Shrinkage.
16. Replace all but the best points with the ones created in the shrinkage operation. Then go to step 3.

4.4 Optimization Results

For each category, the input torque coefficient range from 17 to 27 with a 2 spacing which adds up to a total of 12 cases. The reason we choose this interval is that the lift-to-weight ratio is greater than 1 only when $\hat{M}_{max} > 16.8$ for category B. If $\hat{M}_{max} < 16.8$, the optimization algorithm couldn't find any point of which the objective function (Equation 4.1) is less than 0. Solutions of wing kinematics from optimization are fit using Fourier series to analyze response frequencies, angle amplitudes and phase offsets for characterizing wing kinematics. Fourier series of ϕ, θ and ψ are given by

$$\phi = \phi_0 + \sum_{i=1}^{3} \phi_i \, sin\left(\omega_\phi \, i \, \hat{t} + \alpha_{\phi i}\right), \tag{3.30}$$

$$\theta = \theta_0 + \sum_{i=1}^{3} \theta_i \, sin\left(\omega_\theta \, i \, \hat{t} + \alpha_{\theta i}\right), \tag{3.31}$$

$$\psi = \psi_0 + \sum_{i=1}^{3} \psi_i \, sin\left(\omega_\psi \, i \, \hat{t} + \alpha_{\psi i}\right). \tag{3.32}$$

ω_ϕ, ω_θ and ω_ψ are response frequencies of ϕ, θ and ψ. $\omega_\psi = \omega_\phi = 2\pi$ corresponds to a typical oval shape motion, and $\omega_\psi = 2\omega_\phi = 4\pi$ corresponds to a typical figure-of-eight

motion. Note that all trajectories we obtained here are figure-of-eight pattern. This oscillation system doesn't generate any oval shape trajectories. The response frequency of ϕ is always equal to the driving frequency of the input torque, that is, $\omega_\phi = 2\pi$.

We define the stroke-deviation phase offset β_θ and the stroke-rotation phase offset β_ψ as:

$$\beta_\theta = \alpha_{\theta 1} - \alpha_{\phi 1} \tag{3.33}$$

and

$$\beta_\psi = \alpha_{\psi 1} - \alpha_{\phi 1}. \tag{3.34}$$

Data from the optimization results are listed in Table 4.2 and Table 4.3. Primary parameters of wing kinematics are picked from Fourier series and listed in Table 4.4 and Table 4.5, including frequencies, the firsts term and the first Fourier series of ϕ, ψ and θ. Other series are listed in the Appendix C. We could easily conclude that 6 cases in category A have the almost same optimum wing trajectory, and there is a similar conclusion in category B. The optimal wing motion in category B is a figure-8 shaped with a large stroke deviation (~6°). Additionally, optimal motions are such that they produce nearly above enough lift to hover, and not more (to within $mg \times 10^{-15}$). The lift-to-weight ratios are equal to 1 no matter what the input toque coefficient is. Since additional lift production requires an increase in power consumption, the inequality constraint placed upon the optimization acts more like an equality constraint ($L = 1$ as opposed to $L \geq 1$).

Table 4.2. Optimization parameters with zero deviation.

Symbol	A1	A2	A3	A4	A5	A6	Average
$\hat{M}_{max}$	17	19	21	23	25	27	–
$\hat{k}_{\phi}$	61.21	92.85	113.68	133.55	149.07	167.03	–
$\hat{k}_{\psi}$	21.6	21.3	21.5	21.1	21.9	21.6	21.5
$\hat{k}_{\theta}$	50000	50000	50000	50000	50000	50000	–
$\overline{PL}$ (s/m)	0.3326	0.3318	0.3308	0.3302	0.3293	0.3290	0.3306
L	1.00	1.00	1.00	1.00	1.00	1.00	1.00

Table 4.3. Optimization parameters with nonzero deviation.

Symbol	B1	B2	B3	B4	B5	B6	Average
$\hat{M}_{max}$	17	19	21	23	25	27	–
$\hat{k}_{\phi}$	69.74	97.82	120.24	138.58	155.98	172.47	–
$\hat{k}_{\psi}$	10.56	10.9	11.31	11.60	11.66	11.68	11.29
$\hat{k}_{\theta}$	1212.0	1231.0	1388.6	1424.4	1438.4	1482.8	–
$\overline{PL}$ (s/m)	0.3473	0.3522	0.3546	0.3563	0.3571	0.3573	0.3541
L	1.00	1.00	1.00	1.00	1.00	1.00	1.00

Additionally, the average value of the power loading of the cases without the deviation is 0.3306 s/m, and the value with the deviation is 0.3541 s/m. In category A, the power loadings range from 0.3326 s/m to 0.3290 s/m as $\hat{M}_{max}$ increase. Similar performance exists in category B. The power loadings stay between 0.3473 s/m and 0.3513 s/m. The wing trajectories with nonzero deviation show 7% increase of power loading compared to those with zero deviation. the deviation Many current flapping micro air vehicles (MAV) have limited flight times due to the limited capacity end density of available small-scale power supplies. It is no doubt that the future of MAV depends heavily on improvement of energy sources. Thus this is potentially a favorable feature from the point of view of MAV design and operation.

The oscillatory flapping motions are symmetric in all the cases, and the absolute values of ϕ_0 and ψ_0 are less than 0.002. The average values of ϕ_1, the amplitude of the first Fourier series, are 55.66 degrees for category A and 55.55 degrees for category for category B. It is of interest to find that these values are within the observed range of stroke amplitudes in fruit flies. Some studies suggest that the wing trajectory pattern with a large stroke amplitude and a lower flapping frequency is preferred (Berman and Wang, 2007). This makes sense, as the translational aerodynamic force contributes the most part of the lift the insect need. A larger stroke amplitude allows a larger percentage of the period to be spent in the mid-stroke, where the translational aerodynamic lift is generated. However if the flapping frequency stays constant, a larger power consumption is required for a larger stroke amplitude. Under the driving of input torque with a constant frequency 240 *Hz*, the optimized wing pattern is not the one with 90 degrees stroke, but the one with

55 degrees stroke angel. The insect maybe limits its stroke amplitude by tuning the stiffness of its muscle to achieve a high power efficient wing trajectory pattern. The relationship of input power coefficient and stroke stiffness coefficients is shown in Figure 4.3. The stroke stiffness coefficients from the optimized results increase linearly as the input torque coefficient increases. The stroke stiffness coefficient with non-zero deviation is slight greater than the one with zero deviation.

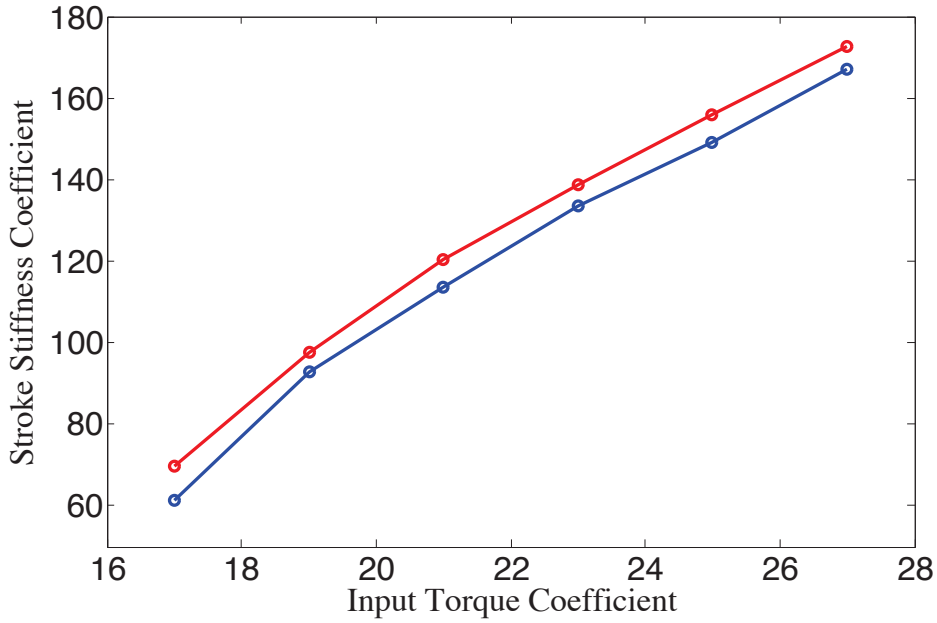

Figure 4.3. Stroke stiffness coefficients versus input torque coefficient. Case A3 is plot in red line and case B3 is plot in blue line.

The average values of ψ_1, the amplitude of the first Fourier series, are 53.62 degrees for category A and 54.96 degrees for category for category B. The rotation angle at about

54 degrees during flapping could maintain a relative constant angle of attack. All of the optimal wing motions in 12 cases are delay rotation.

Table 4.4. Selected Fourier coefficients for optimization wing kinematics results with zero deviation.

Symbol	A1	A2	A3	A4	A5	A6	Average
ω_{ϕ}	6.2832	6.2832	6.2832	6.2832	6.2832	6.2832	6.2832
ω_{ψ}	6.2832	6.2832	6.2832	6.2832	6.2832	6.2832	6.2832
ϕ_0 (deg)	-0.0217	-0.0075	-0.0050	-0.0037	-0.0038	-0.0034	-0.0075
ψ_0 (deg)	-0.0026	-0.0049	-0.0071	-0.0091	-0.0113	-0.0097	-0.0075
ϕ_1 (deg)	54.78	55.41	55.76	56.11	56.01	55.90	55.66
ψ_1 (deg)	52.72	53.58	53.68	54.40	53.54	53.81	53.62
$\alpha_{\phi 1}$ (deg)	-163.53	-149.42	-144.90	-135.70	-132.02	-127.88	–
β_{ψ} (deg)	-102.25	-103.31	-103.29	-104.34	-103.05	-103.76	-10.3.33
θ_{max} (deg)	0.1500	0.1540	0.1567	0.1591	0.1609	0.1607	0.1569
θ_{min} (deg)	-0.0150	-0.0155	-0.0160	-0.0157	-0.0153	-0.0161	-0.0156

Table 4.5. Selected Fourier coefficients for optimization wing kinematics results with nonzero deviation.

Symbol	B1	B2	B3	B4	B5	B6	Average
ω_ϕ	6.2832	6.2832	6.2832	6.2832	6.2832	6.2832	6.2832
ω_ψ	6.2832	6.2832	6.2832	6.2832	6.2832	6.2832	6.2832
ω_θ	12.566	12.566	12.566	12.566	12.566	12.566	12.566
ϕ_0 (deg)	-0.0280	-0.0164	-0.0095	-0.0093	-0.0088	-0.0090	-0.0135
ψ_0 (deg)	0.0003	0.0005	0.0019	0.0062	0.0107	0.0131	0.0055
θ_0 (deg)	2.8	2.7	2.4	2.3	2.3	2.2	2.45
ϕ_1 (deg)	56.12	55.63	55.65	55.40	55.23	55.24	55.55
ψ_1 (deg)	55.13	54.82	55.23	54.91	54.77	54.91	54.96
θ_1 (deg)	3.75	3.72	3.29	3.22	3.20	3.12	3.38
$\alpha_{\phi 1}$ (deg)	-157.62	-144.38	-136.74	-131.51	-127.38	-124.02	–
β_ψ (deg)	-110.33	-108.14	-107.06	-105.64	-104.75	-104.30	–
β_θ (deg)	-14.03	0.54	9.48	16.49	21.79	25.76	–

It should be noted that although small changes exist between cases in each category, the wing kinematics, forces, and powers resulting from the optimization procedure do not

differ qualitatively. We pick the case A3 $\left(\hat{M}_{max}=21,\hat{k}_{\phi}=113.68,\hat{k}_{\psi}=21.5,\hat{k}_{\theta}=50000\right)$ from the category A and the case B3 $\left(\hat{M}_{max}=21,\hat{k}_{\phi}=120.24,\hat{k}_{\psi}=11.31,\hat{k}_{\theta}=1388.6\right)$ from the category B to investigate the effect of the deviation in the following discussion. Wing tip trajectories of optimized wing motions of case A3 and case B3 are shown in Figure 4.4.

The details of the kinematics for optimized wing motions of case A3 and B3 are shown in Figure 4.5. The stroke angle during one wing beat is shown in Figure 4.5 (a). We can see that the trajectories of stroke angles for case A3 and case B3 are almost the same. The trajectories of rotation angles are different, as shown in Figure 4.5 (b). As we discuss in previous sections, aerodynamic forces and moments acting on a wing section are functions local angle of attack α, which is defined as the angle between the wing chord and the direction of local velocity. In the case B3, the local velocity consists of two components, one due to the translational motion and the other due to the motion of the deviation. This indicates the motion of the deviation effect the local angle of attack. The maximum value of the rotation angle in case B3 is slightly greater than the one in case A3. The trajectories of deviation angels are shown in Figure 4.5 (c). Case A3 shows almost zero deviation, as the value of the stiffness coefficient is 50000. The deviation angles are relative small, less than 1 degrees, at the beginning and near the end of the stroke.

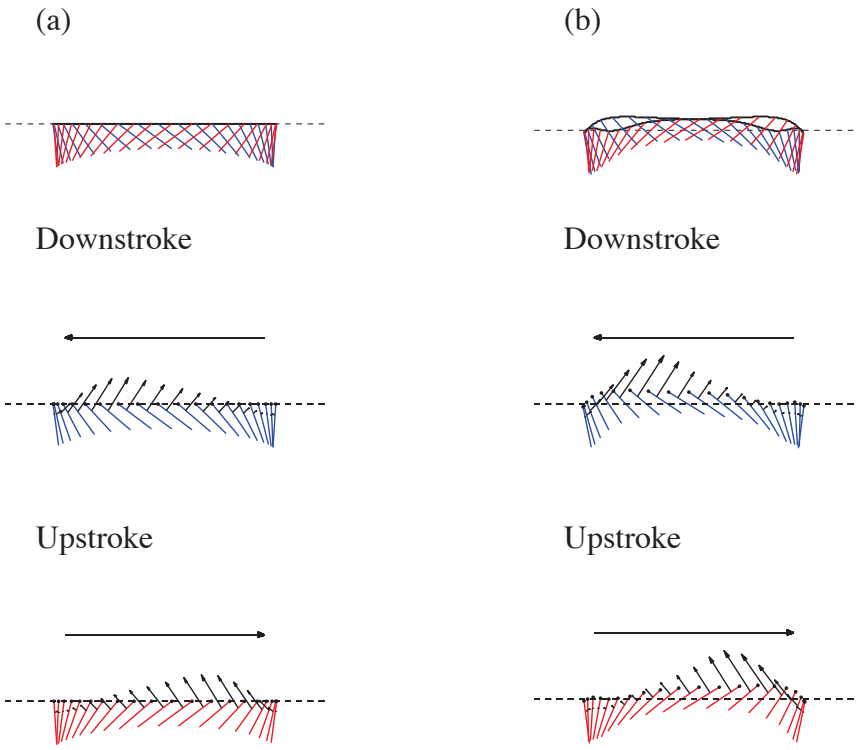

Figure 4.4. Wing trajectories, downstroke phases and upstroke phases of optimized wing motions. Wing cross section snapshots are portrayed and spaced 0.025/1 apart over the 40th stroke cycle. (a) is case A3 and (b) is case B3. The black arrows indicate magnitude and direction of instantaneous forces on the wing.

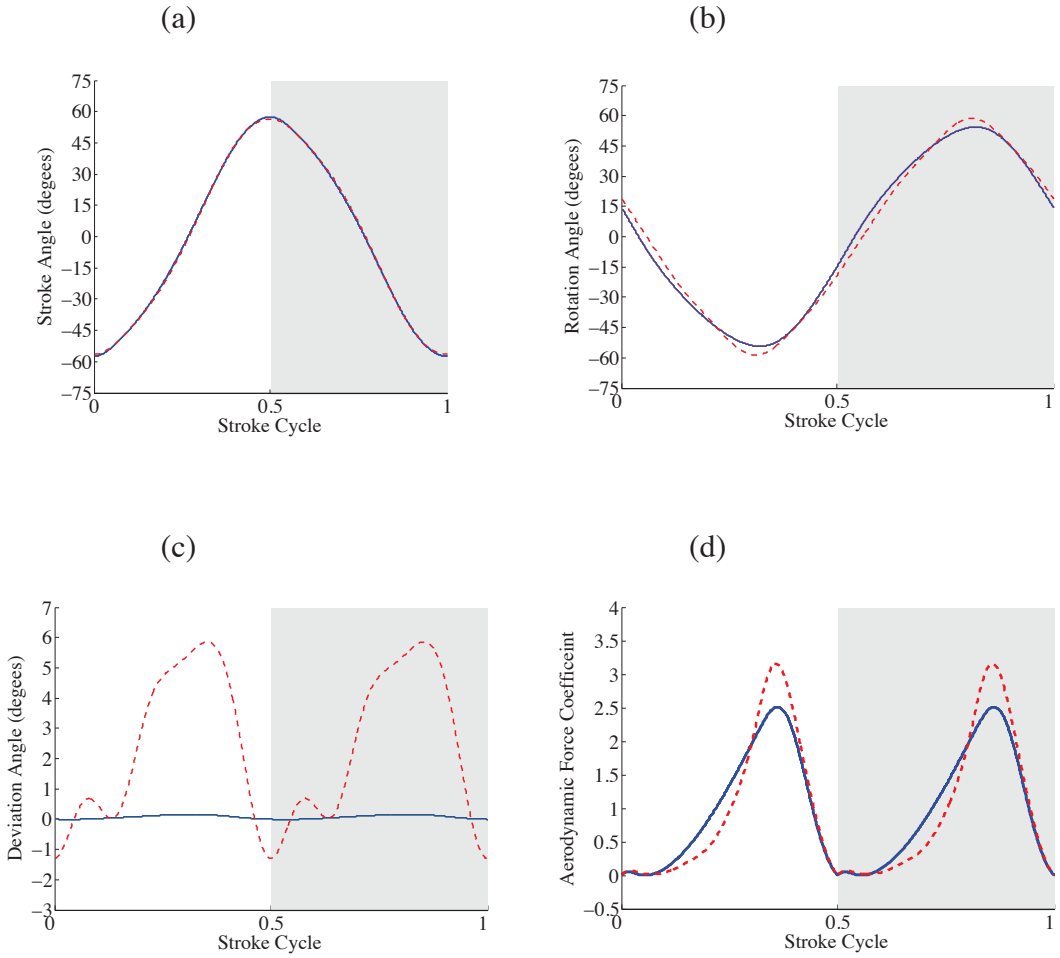

Figure 4.5. Wing kinematics and aerodynamic force coefficient for optimized wing motions versus stroke cycle over the 40th stroke cycle. Wing kinematics of case A3 is plot in solid blue lines, and wing kinematics of case B is plot in dash red lines. The white region indicates the downstroke, and the grey region indicates the upstroke. (a) shows stroke angle v.s. stroke cycle, (b) shows rotational angle v.s. stroke cycle and (c) shows deviation angle v.s. stroke cycle. (d) shows aerodynamic force coefficient v.s. stroke cycle.

CHAPTER 5. CONCLUSION

This study worked towards an integrative understanding of biology system of insect flight muscle, and tried to answer how these muscles drove a flapping wing and how complex fancy wing trajectories were generated. It proposed a simple and effective wing actuation mechanism of flapping micro air vehicles. We started from the two distinct classes of insect flight muscle: power muscles and control muscles, based on which a three DOF oscillation system was developed. The wing was driven under only one actuator, with three torsional springs that were attached on three Euler respectively. The dynamics of the system was then studied using a blade-element model and a quasi-steady model. Four coefficients are defined using non-dimensional analysis. They are stroke stiffness coefficient, rotation stiffness coefficient, deviation stiffness coefficient and input torque coefficient. Simulations showed that tuning stiffness coefficients generated different wing trajectories. A high deviation stiffness coefficient and a mediate rotation stiffness coefficient produced high lift while achieving high power loading. Additionally, an optimization was developed to find optimal wing kinematics that minimized power consumption and provided enough lift to maintain a time-averaged constant altitude over one stroke cycle. The results of this optimization show that the flapping wing with nonzero deviation was better in terms of power. Future work will involve mechanical designs of this oscillation system with three torsional springs.

LIST OF REFERENCES

LIST OF REFERENCES

Andersen, A., Pesavento, U. and Wnag, Z. J., 2005, "Unsteady aerodynamics of flutting and tumbling plates," *Journal of Fluid Mechanics*, vol. 541, pp. 65-90.

Arabagi, B., and Sitti, M., 2008, "Simulation and analysis of a passive pitch reversal flapping wing mechanism for an aerial robotic platform," in *IEEE/RSJ International Conference on Intelligent Robots and Systems*, pp. 1260-1265.

Banala, S. and Agrawal, S, 2005, "Design and optimization of a mechanism for out-of-plane insect winglike motion with twist," *Journal of Mechanical Design*, vol. 127, pp. 841-846.

Balint, C. N. and Dickinson, M. H., 2001, "The correlation between wing kinematics and steering muscle activity in the blowfly *Calliphora vicina*," *Journal of Experimental Biology*, vol. 204, pp. 4213-4226.

Berman, G. J., and Wang, Z. J., 2007, "Eergy-minimizing kinematics in hobering insect flight," *Journal of Fluid Mechanics*, vol. 582, pp. 153-168.

Breugal, F. V., Regan, W. and Lipson, H., 2008, "Demonstration of a passively stable, untethered flapping-hovering micro-air vehicle," *IEEE Robotics and Automation Magazine*, pp. 69.

Brodsky, A. K., 1994, *The Evolution of Insect Flight.* Oxford: Oxford University Press.

Cheng, B., Roll, J. A, Deng, X., 2013, "Modeling and optimization of an electromagnetic actuator for flapping wing micro air vehicle," in *IEEE International Conference on Robotics and Automation*, pp. 4035-4041.

Combes, S. A., and Daniel, T.L., 2003, “Flexural stiffness in insect wings I. Scaling and the influence of wing venation,” *Journal of Experimental Biology*, vol. 206, pp. 2979-2987.

Croon, G. C. H. E. d., Groen, M. A., Wagter, C. D., Remes, B., Ruijsink, R., and Oudheusden, B. W. v., 2012, “Design, aerodynamics and autonomy of the DelFly,” Bioinspiration and Biomimetics, vol. 7, pp. 025003.

Davis, L. 1987, “*Genetic Algorithms and Simulated Annealing*,” Research Notes in Artificial Intelligence. London: Pitman.

Dickinson, M, H., and Tu, M. S., 1997, “The function of Dipteran flight muscle,” *Comparative Biochemistry and Physiology Part A: Physiology*, vol. 116, Issue 3, pp. 223-238.

Dickinson, M. H., Lehmann, F.-O. and Sane, S. P. 1999, "Wing rotation and the aerodynamic basis of insect flight," *Science*, vol. 284, pp. 1881-2044.

Dickinson, M. H., and Lighton, J. R. B., 1995, “Muscle efficiency and elastic storage in the flight motor of *Drosophila*,” *Science*, vol. 268, pp. 87-90.

Dickson, W. B., Straw, A. D., Poelma, C., and Dickinson, M. H., 2006, "An integrative model of insect flight control," in *44th AIAA Aerospace Sciences Meeting and Exhibit*. Reno, NV, USA.

Dormand, J. R., and Prince, P. J., 1980, “A family of embedded Runge-Kutta formulae,” *Journal of Computational and Applied Mathematics*, vol. 6, pp. 19-26.

Dudley, R. *The Biomechanics of Insect Flight: From, Function and Evolution*. Princeton, NJ: Princeton University Press, 1999.

Ellington, C. P., 1984a, “The aerodynamics of hovering insect flight. II. Morphological parameters,” *Philosophical Transactions of the Royal Society of London Series B-Biological Sciences*, vol. 305, pp. 17-40.

Ellington, C. P., 1984b, “The aerodynamics of hovering insect flight. III. Kinematics,” *Philosophical Transactions of the Royal Society of London Series B-Biological Sciences*, vol. 305, pp. 41-75.

Ellington, C. P., 1984c, "The aerodynamics of hovering insect flight .IV. Lift and power requirements," *Philosophical Transactions of the Royal Society of London Series B-Biological Sciences*, vol. 305, pp. 145-181,.

Ellington, C. P., 1999, "The novel aerodynamics of insect flight: applications to micro-air vehicles," *Journal of Experimental Biology*, vol. 202, pp. 3439-3448.

Ennos, A. R., 1989, "The kinematics and aerodynamics of the free flight of some Diptera," *Journal of Experimental Biology*, vol. 142, pp. 49-85.

Finio, B. M., Whitney, J. P., and Wood, R. J., 2010, "Stroke plane deviation for a microrobotic fly," in *IEEE/RSJ International Conference on Intelligent Robots and Systems*, pp. 1889-1894.

Fry, S. N., Sayaman, R., and Dickinson, M. H., 2005, "The aerodynamics of hovering flight in *Drosophila*," *Journal of Experimental Biology*, vol. 208, pp. 2303-2318.

Greenewalt, C. H., 1960, "The wing of insects and birds as mechanical oscillators," *Proceedings of the American Philosophical Society*, vol. 104, pp. 605-611.

Goldberg, D. E., 1989, *Genetic Algorithms in Search, Optimization and Machine Learning*, Addison-Wesley.

Harrison, J. F. and Roberts, S. P., 2000, "Flight respiration and energetics," *Annual Review of Physiology*, vol. 62, pp. 179-205.

Hedrick, T. L. and Daniel, T. L., 2006, "Flight control in the hawkmoth manduca sexta: the inverse problem of hovering," *Journal of Experimental Biology*, vol. 209, pp. 3114-3130.

Hedrick, T. L., Cheng, B, and Deng, X., 2009, "Wingbeat time and the scaling of passive rotational damping in flapping flight," *Science*, vol. 324, pp. 252-255.

Holland, J. H., 1992, "*Adaptation in Natural and Artificial Systems: An introductory Analysis with Applications to Biology, Control, and Artificial Intelligence*," Cambridge, MA: MIT Press.

Jang, J.-S. R., Sun, C.-T., and Mizutani, E., 1997, "*Neuro-Fuzzy and Soft Computing: A Computational Approach to Learning and Machine intelligence*," Upper Saddle River, NJ: Prentice Hall.

Josephson, R. K., 1981, "Temperature and the mechanical performance of insect muscle," *Insect Thermoregulation* (ed. B. Heinrich), pp. 19-44, New York: John Wiley & Sons.

Josephson, R.K., 2006, "Comparative physiology of insect flight muscle," in: Josephson, R.K., Vigoreaux, J.O. (eds.) Nature's Versatile Engine: Insect Flight Muscle Inside and Out, Springer, US, pp. 34–43.

Keennon, M., Klingebiel, K., Won, H., and Andriukov, A., 2012 "Development of the Nano Hummingbird: A Tailless Flapping Wing Micro Air Vehicle," *in 50th AIAA Aerospace Sciences Meeting*, Nashville, Tennessee, USA.

Kora, J. R., 1992, "*Genetic Programming: On the Programming of Computers by Means of Natural Selection*," Cambridge, MA: MIT Press.

Kozek, T., Roska, T., and Chua, L. O., 1993, "Genetic algorithm for CNN template learning," *IEEE Transactions on Circuits and Systems, I: Fundamental Theory and Applications*, vol. 40, no. 6 pp. 392-402.

Lentink, D., and Dickinson, M. H., 2009, "Rotational accelerations stabilize leading edge vortices on revolving fly wing," *Journal of Experimental Biology*, vol. 212, pp. 2705-2719.

Lagarias, J. C., Reeds, J. A., Wright, M. H., and Wright, P. E., 1998, "Convergence properties of the Nelder-Mead simplex method in low dimensions," *SIAM Journal on Optimization*, vol. 9, no. 1, pp. 112-147.

Lehmann, F. –O., 2004, "The mechanisms of lift enhancement in insect flight," *Naturewissenschaften*, vol. 91, pp. 101-122.

Leishman, J. G., 2006, *Principles of Helicopter Aerodynamics*, 2nd edition, Cambridge University Press, New York, NY.

Ma, K, Chirarattanon, P., Fuller, S, and Wood, R. J., 2013, "Controlled flight of a biologically inspired, insect-scale robot," *Science*, vol. 340, pp. 603-607.

MacMahon, T.A., 1984, *Muscles, Reflexes, and Locomotion*, Princeton, NJ: Princeton University Press.

Mitchell, M., 1996, "*An Introduction to Genetic Algorithms*," Cambridge, MA: MIT Press.

Nachtigall, W., and Wilson, D. M., 1967, "Neuromuscular control of dipteran flight," *Journal of Experimental Biology*, vol. 47, pp. 77-97.

Nelder, J. A. and Mead, R., 1965, "A simplex method for unction minimization," *Computer Journal*, vol. 7, no. 4, pp. 308-313.

Pornsin-Sirirak, T., Tai, Y., Ho, C., and Keennon, M., 2001, "Microbat: A Palm-sized electrically powered ornithopter," *Proceedings of NASA/JPL Workshop on Biomorphic Robotics*, pp. 14-17.

Sane, S. P., 2003, "The aerodynamics of insect flight," *Journal of Experimental Biology*, vol. 206, pp. 4191-4208.

Sane, S. P., and Dickinson, M. H., 2001, "The control of flight force by a flapping wing: lift and drag production," *Journal of Experimental Biology*, vol. 204, 2607-2626.

Sane, S. P., and Dickinson, M. H., 2002, "The aerodynamic effects of wing rotation and a revised quasi-steady model of flapping flight," *The Journal of Experimental Biology*, vol. 205, 1087-1096.

Sedov, L. I., 1965. "*Two-Dimensional Problems in Hydrodynamics and Aerodynamics*", pp. 20-30. New York: Interscience Publishers.

Seshadri, Pranay, Benedict, Moble, and Chopra, Inderjit, 2012, "A novel mechanism for emulating insect wing kinematics", *Bioinspiration & Biomimetics*, Vol.7(3), p.036017 (15pp).

Spendley, W., Hext, G. R., and Himsworth, F. R., 1962, "Sequential application of simplex designs in optimization and evolutionary operation," *Technometrics*, bol 48, no. 51, pp. 460-467.

Sun, M., and Tang, J., 2002a, "Unsteady aerodynamic force generation by a model fruit fly wing in flapping motion," *Journal of Experimental Biology*, vol. 205, pp. 55-70.

Sun, M., and Tang, J., 2002b, "Lift and power requirements of hovering flight in Drosophila virilis," *Journal of Experimental Biology*, vol. 205, pp. 2413-2427.

Then, T. W., and Chong, E. K. P., 1994, "Genetic algorithms in noisy environments," in *Proceedings of the 9th IEEE Symposium on Intelligent Control*, pp. 225-230.

Tu, M. S., and Dickinson, M. H., 1994, "Modulation of negative work output from a steering muscle of the blowfly Calliphora vicina," Journal of Experiment Biology, vol. 192, pp. 207-224.

Tu, M. S., and Dickinson, M. H., 1996, "The control of wing kinematics by two steering muscles of the blowfly, (*Calliphora vicina*)," *Journal of Comparative Physiology A*, vol. 178, pp. 813-830.

Viieru, D, Tang, J., Lian, Y., Liu, Hao, and Shyy, W, 2006, "Flapping and flexible wing aerodynamics of low Reynolds number flight vehicles," in *44th AIAA Aerospace Sciences Meeting and Exhibit*. Reno, NV, USA.

Wang, Z. J., 2000, 2000, "Vortex shedding and frequency selection in flapping flight," *Journal of Fluid Mechanics*, vol. 410, pp. 323-341.

Wainwright, S. A., Biggs, W. D., Currey, J. D., and Gosline, J. M., 1982, "*Mechnical Design in Organisms,*" *Princeton*, New Jersey: Princeton University Press.

Weis-Fogh, T., 1973, "Estimates of flight fitness in hovering animals, including novel mechanisms for lift production," *Journal of Experimental Biology*, vol. 59, pp. 169-230.

Whitney, J. P., and Wood, R. J., 2010, "Aeromechanics of passive rotation in flapping flight," *Journal of Fluid Mechanics*, vol. 660, pp. 197-220.

Williams, C. M., and Williams, M. V., 1943, "The flight muscles of *Drosophila replete*," *Journal of Morphology*, vol. 72, pp. 589-599.

Wisser, A., and Nachtigall, W., 1984, "Functional-morphological investigation on the flight muscles and their insertion points in the blowfly *Calliphora erythrocephala* (Insecta, Diptera)," Zoomophology, vol. 104, pp. 188-195.

APPENDICES

Appendix A Non-dimensional Aerodynamic Moment

In the wing-fixed coordinate system *oxyz*, it can be shown that the aerodynamic moment along *x* axis is given by:

$$M_{aero}^{x} = \boldsymbol{e}_x \times \int_0^R \boldsymbol{r}_{cop,tran}(r) \times d\boldsymbol{F}_D(r) + \boldsymbol{e}_x \times \int_0^R \boldsymbol{r}_{cop,tran}(r) \times d\boldsymbol{F}_L(r), \tag{A.1}$$

where

$$d\boldsymbol{F}_D(r) = \frac{1}{2} C_D(\alpha) \rho_{air}\, c(r) r^2 (\omega_z + \omega_x) dr\, \boldsymbol{e}_D, \tag{A.2}$$

$$d\boldsymbol{F}_L(r) = \frac{1}{2} C_L(\alpha) \rho_{air}\, c(r) r^2 (\omega_z + \omega_x) dr\, \boldsymbol{e}_L. \tag{A.3}$$

The aerodynamic moment along *y* axis is given by:

$$M_{aero}^{y} = \boldsymbol{e}_y \times \int_0^R \boldsymbol{r}_{cop,tran}(r) \times d\boldsymbol{F}_D(r) + \boldsymbol{e}_y \times \int_0^R \boldsymbol{r}_{cop,tran}(r) \times d\boldsymbol{F}_L(r) + M_{rd}^{y}, \tag{A.4}$$

where

$$M_{rd}^{y} = -\frac{1}{8} C_{rd} \rho_{air} |\omega_y| \omega_y \overline{c}^4 R \int_0^1 \hat{c}(\hat{r})^4 d\hat{r}. \tag{A.5}$$

The aerodynamic moment along *z* axis is given by:

$$M_{aero}^{z} = \boldsymbol{e}_z \times \int_0^R \boldsymbol{r}_{cop,tran}(r) \times d\boldsymbol{F}_D(r) + \boldsymbol{e}_z \times \int_0^R \boldsymbol{r}_{cop,tran}(r) \times d\boldsymbol{F}_L(r) + M_{rd}^{z}, \tag{A.6}$$

where

$$M_{rd}^{y} = -\frac{1}{6} C_{rd} \rho_{air} |\omega_y| \omega_y \overline{c}^3 R^2 \int_0^1 \hat{c}(\hat{r})^3 \hat{r}\, d\hat{r}. \tag{A.7}$$

Non-dimensional angular velocities are

$$\hat{\omega}_x = \frac{\omega_x}{2\pi}, \tag{A.8}$$

$$\hat{\omega}_y = \frac{\omega_y}{2\pi}, \tag{A.9}$$

$$\hat{\omega}_z = \frac{\omega_z}{2\pi}. \tag{A.10}$$

Dividing equation A.1, A.4 and A.5 by $2\pi f^2 I_{xx}$ and simplifying yields non-dimensional aerodynamic moments:

$$\begin{aligned} M^x_{aero} = {} & 2\pi\, \boldsymbol{e}_x \times \int_0^R \boldsymbol{r}_{cop,tran}(r) \times \left[\frac{1}{2} C_D(\alpha) \rho_{air}\, c(r) r^2 \left(\hat{\omega}_z + \hat{\omega}_x\right) dr\, \boldsymbol{e}_D \right] \\ & + 2\pi\, \boldsymbol{e}_x \times \int_0^R \boldsymbol{r}_{cop,tran}(r) \times \left[\frac{1}{2} C_L(\alpha) \rho_{air}\, c(r) r^2 \left(\hat{\omega}_z + \hat{\omega}_x\right) dr\, \boldsymbol{e}_L \right], \end{aligned} \tag{A.11}$$

$$\begin{aligned} M^y_{aero} = {} & 2\pi\, \boldsymbol{e}_y \times \int_0^R \boldsymbol{r}_{cop,tran}(r) \times \left[\frac{1}{2} C_D(\alpha) \rho_{air}\, c(r) r^2 \left(\hat{\omega}_z + \hat{\omega}_x\right) dr\, \boldsymbol{e}_D \right] \\ & + 2\pi\, \boldsymbol{e}_y \times \int_0^R \boldsymbol{r}_{cop,tran}(r) \times \left[\frac{1}{2} C_L(\alpha) \rho_{air}\, c(r) r^2 \left(\hat{\omega}_z + \hat{\omega}_x\right) dr\, \boldsymbol{e}_L \right] \\ & - 2\pi \frac{1}{8} C_{rd} \rho_{air} \left|\hat{\omega}_y\right| \hat{\omega}_y\, \bar{c}^4 R \int_0^1 \hat{c}(\hat{r})^4\, d\hat{r}, \end{aligned} \tag{A.12}$$

$$\begin{aligned} M^z_{aero} = {} & 2\pi\, \boldsymbol{e}_z \times \int_0^R \boldsymbol{r}_{cop,tran}(r) \times \left[\frac{1}{2} C_D(\alpha) \rho_{air}\, c(r) r^2 \left(\hat{\omega}_z + \hat{\omega}_x\right) dr\, \boldsymbol{e}_D \right] \\ & + 2\pi\, \boldsymbol{e}_z \times \int_0^R \boldsymbol{r}_{cop,tran}(r) \times \left[\frac{1}{2} C_L(\alpha) \rho_{air}\, c(r) r^2 \left(\hat{\omega}_z + \hat{\omega}_x\right) dr\, \boldsymbol{e}_L \right] \\ & - 2\pi \frac{1}{6} C_{rd} \rho_{air} \left|\hat{\omega}_y\right| \hat{\omega}_y\, \bar{c}^3 R^2 \int_0^1 \hat{c}(\hat{r})^3\, \hat{r}\, d\hat{r}. \end{aligned} \tag{A.13}$$

Finally, we obtain

$$M^x_{aero} = 2\pi\, \hat{M}^x_{aero}, \tag{A.14}$$

$$M_{aero}^{y} = 2\pi\ \hat{M}_{aero}^{y}\,, \tag{A.15}$$

$$M_{aero}^{z} = 2\pi\ \hat{M}_{aero}^{z}\,, \tag{A.16}$$

$$\begin{aligned}\hat{M}_{aero}^{x} = {} & \boldsymbol{e}_x \times \int_0^R \boldsymbol{r}_{cop,tran}(r) \times \left[\frac{1}{2} C_D(\alpha)\rho_{air}\ c(r) r^2 \left(\hat{\omega}_z + \hat{\omega}_x\right) dr\ \boldsymbol{e}_D\right] \\ & + \boldsymbol{e}_x \times \int_0^R \boldsymbol{r}_{cop,tran}(r) \times \left[\frac{1}{2} C_L(\alpha)\rho_{air}\ c(r) r^2 \left(\hat{\omega}_z + \hat{\omega}_x\right) dr\ \boldsymbol{e}_L\right],\end{aligned} \tag{A.17}$$

$$\begin{aligned}\hat{M}_{aero}^{y} = {} & \boldsymbol{e}_y \times \int_0^R \boldsymbol{r}_{cop,tran}(r) \times \left[\frac{1}{2} C_D(\alpha)\rho_{air}\ c(r) r^2 \left(\hat{\omega}_z + \hat{\omega}_x\right) dr\ \boldsymbol{e}_D\right] \\ & + \boldsymbol{e}_y \times \int_0^R \boldsymbol{r}_{cop,tran}(r) \times \left[\frac{1}{2} C_L(\alpha)\rho_{air}\ c(r) r^2 \left(\hat{\omega}_z + \hat{\omega}_x\right) dr\ \boldsymbol{e}_L\right] \\ & - \frac{1}{8} C_{rd}\rho_{air} \left|\hat{\omega}_y\right| \hat{\omega}_y\ \overline{c}^4 R \int_0^1 \hat{c}(\hat{r})^4\, d\hat{r}\end{aligned}\,, \tag{A.18}$$

$$\begin{aligned}\hat{M}_{aero}^{z} = {} & \boldsymbol{e}_z \times \int_0^R \boldsymbol{r}_{cop,tran}(r) \times \left[\frac{1}{2} C_D(\alpha)\rho_{air}\ c(r) r^2 \left(\hat{\omega}_z + \hat{\omega}_x\right) dr\ \boldsymbol{e}_D\right] \\ & + \boldsymbol{e}_z \times \int_0^R \boldsymbol{r}_{cop,tran}(r) \times \left[\frac{1}{2} C_L(\alpha)\rho_{air}\ c(r) r^2 \left(\hat{\omega}_z + \hat{\omega}_x\right) dr\ \boldsymbol{e}_L\right] \\ & - \frac{1}{6} C_{rd}\rho_{air} \left|\hat{\omega}_y\right| \hat{\omega}_y\ \overline{c}^3 R^2 \int_0^1 \hat{c}(\hat{r})^3\, \hat{r}\, d\hat{r}\end{aligned}\,. \tag{A.19}$$

Appendix B Contour Plots

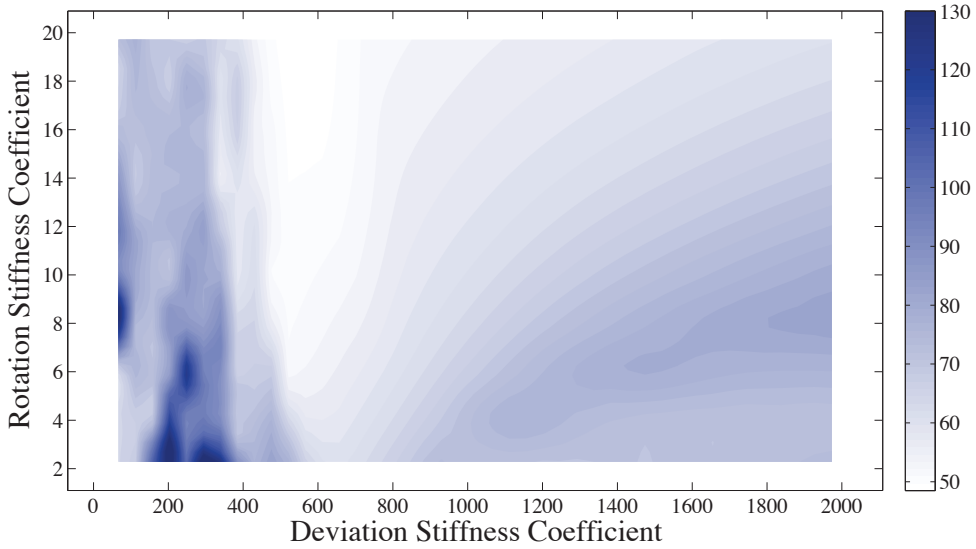

Figure B.1. Contours of amplitude of the stroke angle as functions of deviation stiffness coefficient and rotation stiffness coefficient. Dark shades indicate large values.

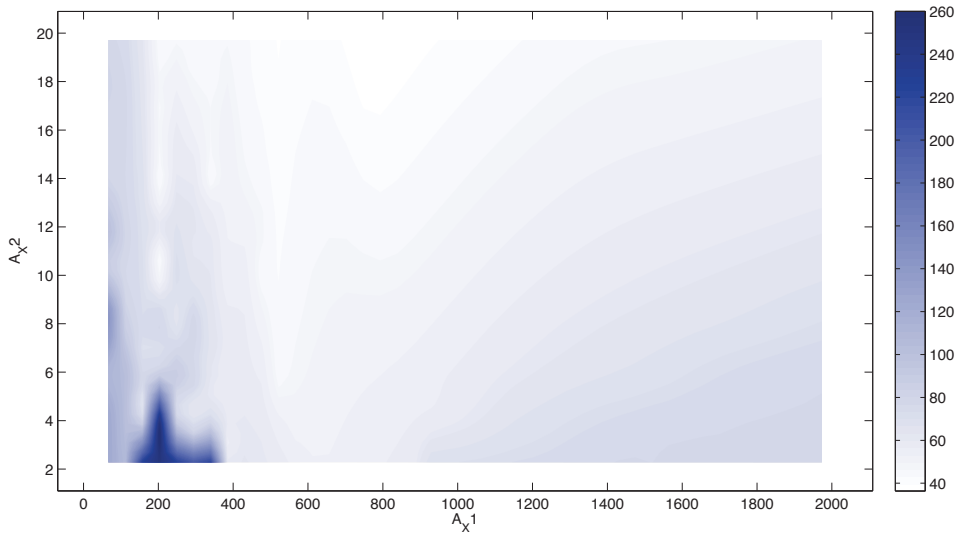

Figure B.2. Contours of amplitude of the rotation angle as functions of deviation stiffness coefficient and rotation stiffness coefficient. Dark shades indicate large values.

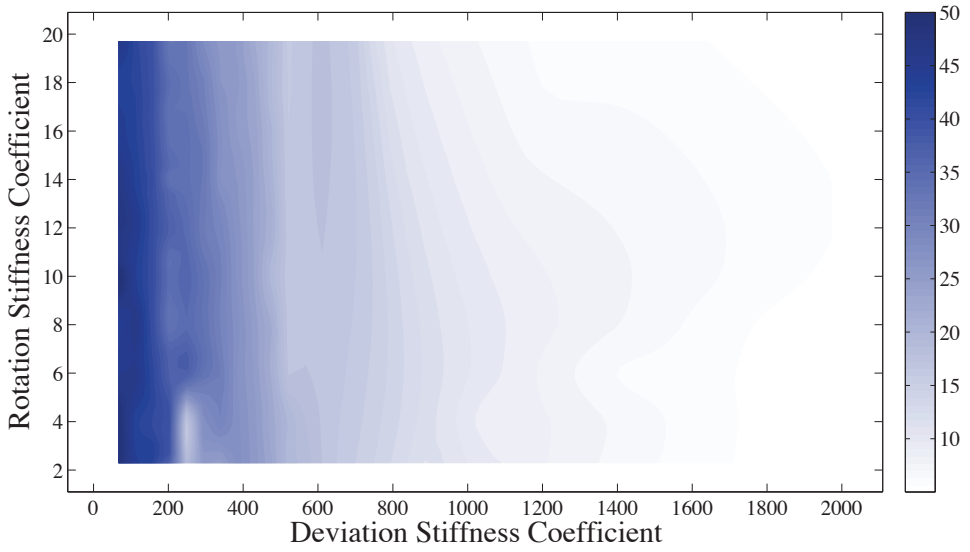

Figure B.3. Contours of amplitude of the deviation angle as functions of deviation stiffness coefficient and rotation stiffness coefficient. Dark shades indicate large values.

Appendix C Fourier Series

Complete Fourier coefficients for 12 cases are list in Table B.1 and Table B.2. For each category, the input torque coefficient range from 17 to 27 with a 2 spacing which adds up to a total of 12 cases.

Table B.1. Fourier coefficients for optimization wing kinematics results with zero deviation

Symbol	A1	A2	A3	A4	A5	A6
ϕ_{max}(deg)	56.31	57.06	57.40	57.86	57.57	57.50
ϕ_{min}(deg)	-56.31	-57.04	-57.36	-57.81	-57.51	-57.43
ϕ_0(deg)	-0.0217	-0.0075	-0.0050	-0.0037	-0.0038	-0.0034
ϕ_1(deg)	54.78	55.41	55.76	56.11	56.01	55.90
$\alpha_{\phi 1}$(deg)	-163.53	-149.42	-144.90	-135.70	-132.02	-127.88
ϕ_2(deg)	0.0164	0.0203	0.0235	0.0263	0.0291	0.0310
$\alpha_{\phi 2}$(deg)	89.19	122.51	140.88	150.44	152.89	154.37
ϕ_3(deg)	1.90	2.17	2.25	2.49	2.32	2.47
$\alpha_{\phi 3}$(deg)	-70.81	-24.84	0.15	20.84	33.77	47.83
ψ_{max}(deg)	53.13	54.13	54.32	55.22	54.36	54.79
ψ_{min}(deg)	-53.20	-54.24	-54.46	-55.38	-54.54	-55.00
ψ_0(deg)	-0.0026	-0.0049	-0.0071	-0.0091	-0.0113	-0.0097

Table B.1. Continued.

Symbol	A1	A2	A3	A4	A5	A6
ψ_1(deg)	52.72	53.58	53.68	54.40	53.54	53.81
$\alpha_{\psi 1}$(deg)	94.22	107.25	114.80	119.96	124.92	128.35
ψ_2(deg)	0.0246	0.0225	0.0256	0.0281	0.0316	0.0336
$\alpha_{\psi 2}$(deg)	-41.02	4.18	15.13	16.70	22.85	25.06
ψ_3(deg)	2.13	2.48	2.66	2.93	2.94	3.15
$\alpha_{\psi 3}$(deg)	-170.01	-128.99	-105.28	-87.42	-73.07	-60.82
θ_{max}(deg)	0.1500	0.1540	0.1567	0.1591	0.1609	0.1607
θ_{min}(deg)	-0.0150	-0.0155	-0.0160	-0.0157	-0.0153	-0.0161
$\hat{\omega}_{\phi}$	6.283	6.283	6.283	6.283	6.283	6.283
$\hat{\omega}_{\psi}$	6.283	6.283	6.283	6.283	6.283	6.283

Table B.2. Fourier coefficients for optimization wing kinematics results with non-zero deviation

Symbol	B1	B2	B3	B4	B5	B6
ϕ_{max}(deg)	57.73	56.35	56.51	55.89	55.44	55.28
ϕ_{min}(deg)	-57.73	-56.35	-56.51	-55.89	-55.44	-55.28
ϕ_0(deg)	-0.0280	-0.0164	-0.0095	-0.0093	-0.0088	-0.0090
ϕ_1(deg)	56.12	55.40	55.65	55.40	55.23	55.24

Table B.2. Continued.

Symbol	B1	B2	B3	B4	B5	B6
$\alpha_{\phi 1}$(deg)	-157.62	-144.38	-136.74	-131.51	-127.38	-124.02
ϕ_2(deg)	0.0158	0.0160	0.0184	0.0203	0.0216	-0.0224
$\alpha_{\phi 2}$(deg)	99.99	126.98	150.16	159.99	166.18	165.76
ϕ_3(deg)	2.42	2.32	2.39	2.27	2.20	2.23
$\alpha_{\phi 3}$(deg)	-44.27	5.50	32.53	54.77	73.04	87.25
ψ_{max}(deg)	56.79	57.63	58.65	58.94	59.38	59.90
ψ_{min}(deg)	-56.81	-57.66	-58.71	-59.00	-59.43	-59.94
ψ_0(deg)	0.0003	0.0005	0.0019	0.0062	0.0107	0.0131
ψ_1(deg)	55.13	54.82	55.23	54.91	54.77	54.91
$\alpha_{\psi 1}$(deg)	92.06	107.48	116.15	122.72	127.70	131.50
ψ_2(deg)	0.0248	0.0175	0.0237	0.0490	0.0657	0.0652
$\alpha_{\psi 2}$(deg)	-59.57	-26.97	68.32	94.78	104.05	107.13
ψ_3(deg)	0.66	1.59	2.18	2.66	3.09	3.47
$\alpha_{\psi 3}$(deg)	-71.04	-37.72	-23.81	-3.24	12.53	23.53
θ_{max}(deg)	6.55	6.52	5.87	5.83	5.86	5.81
θ_{min}(deg)	-1.17	-1.43	-1.31	-1.38	-1.50	-1.53
θ_0(deg)	2.8	2.7	2.4	2.3	2.3	2.2
θ_1(deg)	3.75	3.72	3.29	3.22	3.20	3.12
$\alpha_{\theta 1}$(deg)	-171.64	-143.83	-127.21	-144.92	-150.45	-98.11

Table B.2. Continued.

Symbol	B1	B2	B3	B4	B5	B6
θ_2(deg)	0.67	0.87	0.74	0.76	0.80	0.79
$\alpha_{\theta 2}$(deg)	-54.93	15.24	51.51	81.67	104.70	120.54
θ_3(deg)	0.4673	0.6786	0.8241	0.97	1.11	1.19
$\alpha_{\theta 3}$(deg)	6.10	81.00	149.19	-167.70	-136.29	-107.23
$\hat{\omega}_{\phi}$	6.283	6.283	6.283	6.283	6.283	6.283
$\hat{\omega}_{\psi}$	6.283	6.283	6.283	6.283	6.283	6.283
$\hat{\omega}_{\theta}$	12.566	12.566	12.566	12.566	12.566	12.566

VITA

VITA

Yi Qin
Graduate School, Purdue University

Education
B.S., Mechanical Engineering, 2011, Shanghai Jiao Tong University, Shanghai, China
M.S., Mechanical Engineering, 2014, Purdue University, West Lafayette, Indiana, USA

Research Interests
Dynamic modeling in insect flight.